Yang, Z., Zhong, D., Whitaker, F., Lu, Z., Zhang, S., Tang, Z., Liu, R., & Li, Z. (2019). Syn-sedimentary hydrothermal dolomites in a lacustrine rift basin: petrographic and geochemical evidence from the Lower Cretaceous Erlian Basin, Northern China. *Sedimentology*, [12644]. https://doi.org/10.1111/sed.12644

SYN-SEDIMENTARY HYDROTHERMAL DOLOMITES IN A LACUSTRINE RIFT BASIN: PETROGRAPHIC AND GEOCHEMICAL EVIDENCE FROM THE LOWER CRETACEOUS ERLIAN BASIN, NORTHERN CHINA

ZHE YANG*†, DAKANG ZHONG*†, FIONA WHITAKER§, ZHAO LU¶, SHUO ZHANG**, ZICHENG TANG*, RUNCHAO LIU‡ and ZHUANG LI*

* *College of Geoscience, China University of Petroleum-Beijing, No.18, Fuxue Road, Changping District, Beijing 102249, China* E-mail address: zhongdakang@263.net; yangzhe_cup@126.com

† *State Key Laboratory of Petroleum Resources and Prospecting, China University of Petroleum-Beijing, No.18, Fuxue Road, Changping District, Beijing 102249, China*

§ *School of Earth Sciences, University of Bristol, Wills Memorial Building, Queen's Road, Bristol BS8 1RJ, UK*

¶ *Sinopec Star CO., LTD., No.263, Beisihuan Zhonglu, Haidian District, Beijing 100083, China*

***Tianjin Geothermal Development CO., LTD., Hongqi Nanlu, Nankai District, Tianjin 300110, China*

‡ *Key Laboratory of Orogenic Belts and Crustal Evolution, School of Earth and Space Sciences, Peking University, No.5, Yiheyuan Road, Haidian District, Beijing 100871, China*

Associate Editor – Cathy Hollis

Short Title – Syn-sedimentary hydrothermal dolomite in the Erlian Basin

ABSTRACT

Dolomites occur extensively in the lower Cretaceous along syn-sedimentary fault zones of the Baiyinchagan Sag, westernmost Erlian Basin, within a predominantly fluvial-lacustrine sedimentary sequence. Four types of dolomite are identified, associated with hydrothermal minerals such as natrolite, analcime and Fe-bearing magnesite. The finely-crystalline dolomites consist of anhedral to subhedral crystals (2 to 10 μm), evenly commixed with terrigenous sediments that occur either as matrix supporting grains (Fd1) or as massive argillaceous dolostone (Fd2). Medium-crystalline (Md) dolomites are composed of subhedral to euhedral crystals aggregates (50 to 250 μm) and occur in syn-sedimentary deformation laminae/bands. Coarse-crystalline (Cd) dolomites consist of non-planar crystals (mean size >1 mm), and occur as fracture infills crosscutting the other dolomite types. Fd1, Md and Cd dolomites have similar values of $\delta^{18}O$ (−20.5 to −11.0 ‰ Vienna PeeDee Belemnite) and $\delta^{13}C$ (+1.4 to +4.5 ‰ Vienna PeeDee Belemnite), but Fd2 dolomites are isotopically distinct ($\delta^{18}O$ −8.5 to −2.3‰ Vienna PeeDee Belemnite; $\delta^{13}C$ +1.4‰ to +8.6‰ Vienna PeeDee Belemnite). Samples define three groups which differ in light rare-earth elements *vs*. high rare-earth elements enrichment/depletion and significance of Tb, Yb and Dy anomalies. Md dolomites have signatures that indicate formation from brines at very high temperature, with salinities of 11.8 to 23.2 eq. wt. % NaCl and T_h values of 167 to 283°C. The calculated temperatures of Fd1 and Cd dolomites extend to slightly lower values (141 to 282°C), while Fd2 dolomites are distinctly cooler (81 to 124°C). These results suggest that the dolomites formed from hydrothermal fluid during and/or penecontemporaneous with sediment deposition. Faults and fractures bounding the basin were important conduits through which high-temperature Mg-rich fluids discharged, driven by an abnormally high heat flux associated with local volcanism. It is thought that differing amounts of cooling and degassing of these hydrothermal fluids, and of mixing with lake waters, facilitated the precipitation of dolomite and associated minerals, and resulted in the petrographic and geochemical differences between the dolomites.

Keywords: Early Cretaceous, Erlian Basin, hydrothermal dolomite, lacustrine dolomite, primary dolomite, rift setting, syn-sedimentary dolomite

INTRODUCTION

For more than two centuries, the “dolomite problem” has remained one of the most disputed topics in sedimentary research. Studies suggest that dolomites form in two main realms: either sedimentary or hydrothermal environments. Various mechanisms for early dolomitization have been proposed, both primary microbial and early replacement by sea water-derived fluids, including tidal pumping, sub-mixing zone circulation and brine reflux (e.g. *Kaufman et al., 1991; Whitaker & Smart 1993; Jones et al., 2004; Machel, 2004; Nader et al., 2004; Deng et al., 2010*). However, in recent years many studies have focused on the formation of hydrothermal dolomites in marine and continental environments (e.g. *Machel and Lonnee, 2002; Lavoie et al., 2010; Lapponi, et al., 2014*). This is motivated by their implications for understanding ancient hydrothermal activity, their potential as hydrocarbon reservoirs (e.g. *Dong et al., 2016; Mansurbeg et al., 2016; Feng et al., 2017*) and as hosts to Mississippi Valley-Type lead-zinc mineralization (e.g. *Leach and Sangster, 1993; Hendry et al., 2015; Wei et al., 2015*). In most cases, hydrothermal dolomites form near faults developed in extensional tectonic settings, where faults provide pathways for hydrothermal fluids (e.g. *Vandeginste et al., 2012; Martín-Martín et al., 2013; Martín-Martín et al., 2015; Hollis et al., 2017*). Hydrothermal dolomite is generally considered as a post-depositional product, forming from hydrothermal fluids (hotter than ambient rock) by replacement of precursors including limestones or preexisting dolomites, or by infilling of vugs and fractures (*Machel and Lonnee, 2002; Lonnee and Machel, 2006*). However, a few studies of modern hydrothermal systems suggest that primary dolomites can precipitate from a mixture of hydrothermal fluids and sea water or lake water (e.g. *Barnes and O’Neil, 1971; Eickmann et al., 2009*). Considerable controversy remains as to whether massive primary dolomites can be produced directly from hydrothermal fluids.

There have been very few prior studies of the massive dolomites within the Cretaceous Tengger

Formation in the Erlian Basin. Based on previous studies (*Guo et al., 2012; Zhong et al., 2015*), these dolomites are distinguished by a range of features which suggest their formation relates to hydrothermal processes. Firstly, the dolomites are interbedded, or mixed with normal lacustrine sediments (mainly mudstone and siltstone) and, secondly, they are associated with several high-temperature minerals (e.g., natrolite, analcime) rarely seen in dolomites. These observations have led to a hypothesis that the dolomites are synsedimentary, formed as primary lacustrine precipitates associated with discharge of hydrothermal fluids into a lake basin. This study builds on this work and offers the first detailed investigation of the petrographic texture and geochemical composition of these lacustrine dolomites in the Erlian Basin. It is also a clear example of research into the genesis of dolomites in a continental rift basin in China that examines the interaction between hydrothermal activities and sedimentary process. This mechanism has been suggested for similar dolomites in other continental basins of China, including the Santanghu, Jiuquan and Bohaiwan basins (*Zheng et al., 2006; Liu et al., 2010, 2011; Li et al., 2012a, b; Wen et al., 2014; Song et al., 2015; Jiao et al., 2018*). Understanding the formation and distribution of these dolomites is important because they are important as hydrocarbon reservoirs.

This study aims to document the petrographic and geochemical characteristics of Tengger Formation dolomites, to understand the reasons behind their characteristic variations, and to elucidate their genetic origins. To achieve this, it is performed by: (i) petrographic examination; (ii) stable oxygen and carbon isotope analysis; (iii) rare-earth element analysis; and (iv) fluid-inclusion studies on dolomite samples from the Baiyinchagan Sag in the westernmost part of the Erlian Basin.

GEOLOGICAL SETTING AND STUDY AREA

The Erlian Basin is a Mesozoic continental rift basin sitting on folded Hercynian basement in northern China (*Dou et al., 1998*；*Huang et al., 2003*；*Li et al., 2012*) (Fig. 1A). During the Late Jurassic and Early Cretaceous, the area experienced the subduction of the Pacific Plate under the Eurasian Plate, accompanied by powerful volcanism. This volcanism is represented in the basin by andesite, pyroclastic rocks, tuffs and related rocks (*Ren et al., 1998; Xiao and Yang., 2001; Lu et al., 2011; Ji et al., 2012; Li et al., 2014*). The Baiyinchagan Sag is located in the westernmost part of the basin and covers an area of 3,200 km^2 and can be subdivided into three parts: the eastern sub-sag, the low Maohu uplift and the western sub-sag (Fig. 1B). The sag has undergone a complex evolution involving repeated subsidence and uplift events associated with the multiple tectonic cycles recorded within the basin. The main phase of syn-rift deposition in the Baiyinchagan Sag occurred during the Early Cretaceous and comprised a series of fluvial-lacustrine sediments, which lie unconformably on Jurassic volcanic basement. From bottom to top, the Cretaceous strata include the Arshan Formation (K_1a, ~ 250 to 1300 m), the Tengger Formation (K_1t, ~ 90 to 830 m), the Duhongmu Formation (K_1d, ~ 220 to 1550 m) and the Saihantala Formation (K_1s, ~ 0 to 300 m), which comprise mainly dark terrigenous detrital sediments (Fig. 1C) (*Huang et al., 2003*).

The main study area is located in the southwestern part of the western sub-sag, which is elongated NW–SE, and extends ~20 km in length with a width of ~10 km. The study area is bounded by the ENE–WSW trending Tala fault zone and the NE–SW trending Chagan–Wente fault zone, resulting in the formation of an asymmetric half-graben (Fig. 1D). These two sets of fault zones are composed of a series of normal faults and remained active until the end of the Early Cretaceous (*Deng, 2006*). They developed upwards from the basement and appear to have fundamentally controlled processes of lacustrine deposition. The present study was conducted mainly in the Tengger Formation, which can be subdivided into the Lower and Upper Members. The Lower Member consists of clastic sedimentary rocks, mainly conglomerates, sandstones and mudstones. The Upper Member is composed of argillaceous dolomite, dolomitic mudstone, siltstones and mudstones.

SAMPLES AND ANALYTICAL METHODS

More than fifty wells have been drilled into the Tengger Formation in the Baiyinchagan Sag from which detailed well-logging information is available. Some 312 m of dolomite of the Tengger Formation were examined and described from eight cored wells *(X2*, *X26*, *X31*, *X32*, *X36*, *X3-69, C36 and C39*; Table S1; Fig. 2) preserved in library of the Zhongyuan Oil Field. All the cores are located in the Upper Member of the Tengger Formation, with a total of 185 core samples being collected and analyzed to calibrate data from wireline logs in the cored intervals (Fig. 3). All core samples were carefully examined and 93 samples were selected for thin sections. Based on the petrographic results, representative samples were further selected for microprobe and geochemical analysis.

The thin sections were cut to a standard thickness of 0.03 mm, polished and stained with Alizarin Red-S and potassium ferricyanide (*Dickson, 1966*), and analyzed under a Leica PM4500 polarizing microscope (Leica, Wetzlar, Germany). Cathodoluminescence (CL) microscopy was performed using a CL8200MK5-2 (CITL company, Hatfield, UK) instrument with a 17-kV beam and a current intensity of 300 to 500 μA. Textural characteristics of dolomite and associated mineral assemblages were investigated in detail with a scanning electron microscope (SEM) Quanta 200 FEI with a dispersive X-ray spectrometer (EDS) (FEI Company, Hillsboro, OR, USA). Petrographic microscopy, CL and SEM were conducted at the China University of Petroleum, Beijing. Analysis of major-element composition of minerals was carried out by electron probe micro analysis (EPMA) using an electron microprobe EPMA-1600 (15-kV, beam size 1×10^{-8} Å, beam spot size 1μm, correction ZAF, standard GB/T 115, 074-2008; Shimadzu Corporation, Beijing, China) in the Laboratory of Geoanalysis and Geochronology of Geological Research Centre, Tianjing, China.

The different types of dolomites were sampled for oxygen and carbon isotopic and rare-earth element analyses using a two-speed rotary tool to extract the desired quantity of powdered dolomite after carefully targeting apparently homogeneous areas of each thin section. For oxygen and carbon isotopic analysis, approximately 5 mg of micro-drilled dolomite was reacted with pure phosphoric acid for 12 h at 50°C. The resultant CO_2 was analyzed for its oxygen and carbon isotopic ratios using a Finnigan-MAT252 gas-isotope mass spectrometer (Thermo Fisher Scientific, Waltham, MA, USA) at the University of Petroleum, Beijing. The results based on replicate analyses of GBW 04405, are given using conventional $\delta^{13}C$ and $\delta^{18}O$ notations with respect to the Vienna PeeDee Belemnite (VPDB) standard, with an analytical error of ± 0.1‰.

Rare-earth element (REE) contents were measured using a NexION300D ICP-MS (PerkinElmer Inc., Waltham, MA, USA) at the Beijing Research Institute of Uranium Geology (BRIUG). Approximately 2 mg of sample powder was reacted with 2.5% HNO_3. Precision was in the range 5 to 10%, and the element detection limit was 0.002 ppm. REE concentrations were normalized to NACS (North American Composite Shale; *Gromet et al., 1985*). Anomalies of europium, $(Eu/Eu^*)_{SN} = Eu_{SN}/(0.67Sm_{SN} + 0.33Tb_{SN})$ and cerium, $(Ce/Ce^*)_{SN} = Ce_{SN}/(0.5La_{SN} + 0.5Pr_{SN})$ were calculated according to the formulae of *Bau and Dulski* (*1996*).

Fluid-inclusion microthermometry was performed on doubly polished thin sections using a Linkam mK 1000 heating-freezing stage calibrated using synthetic fluid-inclusion standards at the Petroleum Geology Research and Central Laboratory, Beijing. Homogenization temperatures (T_h) and ice melting temperatures (T_m) were measured according to the procedures of *Shepherd et al.* (*1985*). The accuracy of T_h and Tm is within 3°C and 0.5°C, respectively. Salinity estimates were calculated by applying the measured Tm values to the equation of *Bodnar* (*1993*), and reported as equivalent weight percent NaCl (eq. wt. % NaCl).

LITHOSTRATIGRAPHIC FEATURES AND OCCURRENCE OF DOLOMITE

Logging data and core observation indicated that the Upper Member of Tengger Formation is a mixed sedimentary sequence of argillaceous dolomite, dolomitic mudstone, mudstone, siltstone and rare sandstone (Fig. 3). In well logs, rocks containing dolomite are electrically characterized by natural gamma (GR, ~ 300 to 1500 API) which is significantly higher than that of the normal terrigenous sediments (GR, <250 API) in the study area (Fig. 3). In addition, rocks containing dolomite are locally identified by ultra-high and ultra-low deep resistivity (ILD, ~0.2 to 2000 Ω·m) (Fig. 3). Combining log data with observation of cores, four lithological units from bottom to top can be defined in the Upper Member of the Tengger Formation on the basic of their lithological association (Fig. 2): Unit I is 40 to 170 m thick and is a mixture with highly variable amounts of argillaceous dolomite, dolomitic mudstone and mudstone/siltstone; Unit II is 100 to 190 m thick and is dominated by argillaceous dolomite and dolomitic mudstone locally intercalated mudstone; Unit III is 70 to 150 m thick and is characterized by frequent alternation of dolomite and mudstone/siltstone; Unit IV is 40 to 150 m thick and is dominated by mudstone, with thin beds of dolomite at the top of the unit in many wells. In each unit, rocks containing dolomite mainly show unique structures, like white grains, laminae and band, and breccia, which markedly distinguish from dark colour lacustrine clastic rocks (Fig. 3). Dolomites and lacustrine clastic rocks appear alternately, indicating that the sedimentary environment changed dramatically at that time.

The occurrence of dolomites in the Upper Member of the Tengger Formation is proximal to the fault zones and developed on the footwall blocks of normal faults (Figs 2 and 3). The thickness of dolomite in the NW-SE cross-section is shown to decrease from the faults towards the centre of the basin, although the total stratigraphic thickness increases (Fig. 3). It is also apparent that the dolomite bodies have mounded geometries and gradually thin then pinch out into the surrounding mudstone. The dolomite bodies appear to be elongated NE–SW, parallel to the fault zones (Fig. 2). Their precise dimensions are difficult to assess because the single layer of dolomite-bearing rock is too thin and there is a lack of obvious contacts between dolomite-bearing rock and terrigenous sediments, but the total thickness of dolomite-bearing rocks reaches a maximum of 320 m and dolomite-bearing rock extends for several thousands of square kilometers over the study area (Fig. 2).

PETROGRAPHIC FEATURES OF DOLOMITE

Based on observations of structure, texture and mineral composition in argillaceous dolomite and dolomitic mudstone, four types of dolomite can be identified. However, information on the abundance and occurrence of each type of dolomite at a larger scale is not available because of observations are limited to cores. In the following section the petrographic characteristics of these dolomites are described in order of decreasing abundance.

Fine-crystalline (Fd1 and Fd2) dolomite

Fd1 dolomite (26 to 37%) occurs mixed with very fine terrigenous feldspar (7 to 37%), analcime and natrolite (8 to 19%) and/or minor amounts of illite (＜10%), as a dark-grey matrix supporting a mass of white grains (Fig. 4A to D). Fd1 dolomite deposits have a thickness ranging from centimetres to several metres. Grains are scattered throughout the matrix, but with the long axis of the white grains often oriented normal to the bedding planes (Fig. 4A to D). The grains vary in shape and may be irregular and elongate (Fig. 4A and B), small and spherical (Fig. 4C), or droplet–shape with a small tail (Fig. 4D). They range in size from coarse–grained (>1 mm) to fine–grained (<5 μm). In some cases, grains are wrapped around by depositional laminae (Fig. 4F), indicating a syn-sedimentary relationship between grains and laminae. The major components of these grains are natrolite, with euhedral crystals up to 200 μm long and 50 μm wide (Fig. 4F and G), and/or analcime with octahedral crystals of 10 to 200 μm diameter (Fig. 4H and I). Secondary components include radiaxial-fibrous Fe-bearing magnesite, cubic pyrite and/or subhedral-euhedral dolomite (Fig. 4F, H, I and J), which replaces natrolite and analcime, and rare occurrences of barite within the intracrystalline pores of natrolite grains (Fig. 4K).

Fd2 dolomite (25 to 36%) also occurs mixed with fine terrigenous feldspar (25 to 44%), natrolite and analcime (6 to 37%) and illite (＜10%) to form finely laminated or massive dolomitic mudstone (Fig. 4E). These dolomitic mudstones form layers up to several metres in thickness which can be difficult to differentiate from overlying or underlying mudstones.

Although Fd1 and Fd2 dolomites show different rock structures, they are microcrystalline, with a crystalline size range of 2 to 10 μm (Fig. 4F, H and L). SEM observations indicate that crystals are anhedral to subhedral (Fig. 4M), and sometimes spherical. CL reveals the presence of slightly luminescent Fd2 dolomite with a non-dull-red colour (Fig. 4N), while Fd1 dolomite shows no luminescence. The fine terrigenous feldspar, which commonly appears synchronic and concordant with the fine-crystalline dolomites, is general anhedral and ranges in size from 2 to 10 μm (Fig. 4M), and the majority are albite with a small amount of K-feldspar. There is no petrographic evidence of primary replacement fabrics, or of dissolution/replacement of fine-crystalline dolomite.

Medium-crystalline (Md) dolomite

Md dolomite occurs as white or light-yellow laminae (from several µm to mm thick) which alternate with dark-grey laminae composed of terrigenous sediments and are interlayered with dark-grey mudstone (Fig. 5A and B). The dark-grey laminae are dominated by fine albite and minor amount of K-feldspar. In most cases, the white laminae show small (cm) scale folding and faulting as a result of plastic and soft sediment deformation in an unconsolidated to semi-consolidated deposit (Fig. 5A and B). Md dolomite is present in white bands several cm in thickness, which also show evidence of soft deformation and movement induced by syn-sedimentary fracturing (Fig. 5C and D). Locally, the white consolidated laminae and bands are broken to form irregular breccia of varied size (Figs 4B, 5C and D), comparable to syn-depositional brecciation textures described by *Selleck* (*1978*).

Md dolomite is made up of interlocking subhedral to euhedral crystal aggregates with a size range of 50 to 250 µm, with poorly defined individual crystal boundaries (Fig. 5E, F, G and H). Md dolomites are slightly stained by Alizarin Red-S and K-ferricyanide indicative of a high iron content (not in Fd dolomites due to their small size). These dolomite crystals show a unique internal structure with no alternating rims and display no luminescence (Fig. 5I). Calcite is observed between the dolomite crystals as an intercrystalline pore infill, and consists of dull luminescent sparry crystals (Fig. 5I). Natrolite and analcime are generally replaced by Md dolomites in the white laminae and bands (Fig. 5E, F and J). Compared with the laminae, the bands contain more Md dolomite, but less natrolite, analcime and calcite.

Coarse-crystalline (Cd) dolomite

Cd dolomite fills fractures that crosscut the bedded Fd and Md dolomites indicating they are a later phase of dolomitization. This type of dolomite is easily distinguished by its white colour, contrasting with the dark-grey colour of other dolomites, and forms irregular masses in pores and voids (Fig. 6A). However, the Cd dolomite was identified in only one of the eight wells studied and occurs over a length of <0.5 m of the core.

Cd dolomite is composed of multiple individual, cloudy, non-planar dolomite crystals, with a mean size of >1 mm (Fig. 6B and C). The dolomite is lightly stained by Alizarin Red-S and K-ferricyanide. Under cross-polarized light, the dolomite crystals are characterized by typical undulatory extinction comparable with that of the saddle dolomite described by *Nader et al. (2004)* and *Haeri-Ardakani et al. (2013)*. However, these crystals exhibit non-luminescence under CL, and show no cloudy centres and clear rims or more complex zonation. There are scattered sub-millimetre-sized intercrystalline pores between the Cd crystals (Fig. 6B), and a small amount of analcime and radiaxial-fibrous Fe-bearing magnesite intergrown with the Cd dolomites (Fig. 6C).

GEOCHEMICAL FEATURES OF DOLOMITE

Major-element composition

Major-element composition of CaO, MgO and FeO was determined by electron probe micro-analysis (EPMA) to characterize different types of dolomite (Fd1, Fd2, Md and Cd dolomite) (Table 1), and are plotted in Fig. 7. All dolomites have >1.6 wt. % FeO and are defined as ferroan dolomite (*Tucker and Wright, 1990*). Fd1 and Fd2 dolomites have a similar composition, forming a group (n=29) with 24.92 ± 1.57 wt. % CaO, 14.37 ± 1.46 wt. % MgO and 7.65 ± 1.71 wt. % FeO contents (Fig. 7A and B). Compared to Fd1 and Fd2 dolomites, Cd dolomites show a slightly higher content of CaO (mean 26.50 ± 2.28 wt. %, n=17) and MgO (mean 15.44 ± 1.66 wt.%, n=17) (Fig. 7A), but have a very similar FeO content (mean 7.68 ± 1.23 wt. %, n=17) (Fig. 7B). Interestingly, Md dolomites are chemically distinct from the other dolomites, with the highest CaO content (mean 26.84 ± 1.51 wt. %, n=35) and MgO content (mean 18.10 ± 1.24 wt. %, n=35) and the lowest FeO content (mean 4.47 ± 1.08 wt. %, n=35) (Fig. 7A and B). Md dolomite displays a significantly higher Mg/Ca ratio (mean 0.94 ± 0.04, n=35) than the Fd1, Fd 2 and Cd dolomites (0.81 ± 0.06, n=46), despite also having a lower FeO content. The inverse relationship between FeO and MgO may reflect the ease with which Fe^{2+} substitutes for Mg^{2+} rather than Ca^{2+} (*Gregg et al., 2015*).

Oxygen and carbon isotopes

The $\delta^{13}C$ values of all types of dolomite lie within a narrow range (+2‰ to +4‰), with the exception of Fd2 dolomite, which extend to much heavier $\delta^{13}C$ values. In contrast, the $\delta^{18}O$ values for the dolomites are spread over a relatively wide range (Table 2; Table S2). Based on their $\delta^{18}O$ and $\delta^{13}C$ values, the different types of dolomites can be divided into two groups (Fig. 8). Fd2 dolomites have the highest isotopic values, with $\delta^{18}O$ values of −8.5 to −4.3‰ (mean −6.8 ± 1.5 ‰, n=5) and $\delta^{13}C$ values of +1.4‰ to +8.6‰ (mean +4.9 ± 2.5 ‰, n=5) (Fig. 8). In comparison, the isotopic values for Fd1 and Md dolomites are very similar, forming a group (n=19) with lower $\delta^{18}O$ values (mean −14.3 ± 2.5‰) and lower $\delta^{13}C$ values (mean 3.1 ± 0.9‰) (Fig. 8). $\delta^{18}O$ and $\delta^{13}C$ values for Cd dolomites lie within the range of values for Fd1 and Md dolomites, −16.4 to −14.2‰ and from +3.2 to +3.9‰, respectively (Fig. 8). In addition, two samples of dolomite cement in the mudstone shows very different isotopic values, with a $\delta^{18}O$ value of −4.5 to −3.4‰ and $\delta^{13}C$ value of −4.6 to−2.0‰ (Fig. 8).

Rare-earth elements (REE)

REE concentration of the Upper Formation of the Tengger Formation dolomites and normal mudstone is summarized in Table 2, whereas the NASC-normalized (*Gromet et al., 1985*) REE profiles of dolomites and mudstone is shown in Fig. 9.

Fd1 and Fd2 dolomites have similar ΣREE contents and wide ranges of values relative to the other types of dolomite (Table 2), with mean respective total ΣREE contents of 214.08 ppm (range 135.15 to 328.08 ppm) and 212.14 ppm (range 151.14 to 307.56 ppm). For the ratio of La_N/Yb_N, a wide range of Fd1 and Fd2 dolomites (n=7) have moderate values ranging 1.02 to1.86, but a smaller subset with higher values ranging 2.22 to 3.27 (n=6) indicates light rare-earth element (LREE) enrichment (*Kučera et al., 2009; Wen et al., 2014*). From the REE_N pattern (Fig. 9A), Fd1 and Fd2 dolomites appear to be enriched in LREEs with a slight right-inclining distribution, and slight high rare-earth element (HREE) depletion with a fluctuating HREE distribution, and display slightly positive Tb and Yb anomalies, and a slightly negative Dy anomaly. Conversely, ΣREE contents of

Md dolomites lie in a relatively narrow range of 126.13 to 180.81 ppm (mean 158.32 ppm) and they show a pronounced HREE enrichment ($La_N/Yb_N = 0.54$ to 1.0). The REE_N profile of Md dolomites exhibit pronounced LREE depletion with a slight left-inclining distribution, and HREE enrichment with a flat HREE distribution, and display slightly positive Tb and Yb anomalies, except for one sample which has pronounced positive Eu and Gd anomalies (Fig. 9B). The two samples of Cd dolomite yield the lowest ΣREE contents with mean value of 93.23 ppm and show a slight LREE enrichment ($La_N/Yb_N = 1.39$ to 1.93). The REE_N profile of Cd dolomite shows slight LREE enrichment with a flat distribution, and a slight HREE depletion with a weak right-inclining distribution, and displays pronounced positive Eu and Tb anomalies and negative Dy and Er anomalies (Fig. 9C). No dolomite types show a positive Eu anomaly (Eu/Eu* mean 0.89) except for Cd dolomite, which has a slightly positive Eu anomaly (Eu/Eu* mean 1.21), and all exhibit a very slightly negative Ce anomaly (Table 2).

Mudstone in the study area, considered as the background lacustrine sediment, yields stable ΣREE content ranging from 203.20 to 257.21 ppm (mean 233.64 ppm). The mean of La_N/Yb_N ratio is 1.30 suggesting a weak HREE enrichment. The mudstones show a relatively flat REE distribution with slight HREE depletion, with a slightly negative Eu and positive Yb anomalies (Fig. 9D).

Fluid-inclusion microthermometry

Microthermometric measurements focused on primary two-phase (liquid and vapour) fluid inclusions from the dolomites. Because of their small size, fine-crystalline dolomites are not suitable for microthermometry. Fluid inclusions from Md dolomites show irregular to elongate shapes with a size range of 4 to 12 µm (Fig. 10A). These have a wide range of homogenization temperature (T_h) from 167 to 283°C, but a negatively skewed distribution with 55% yielding temperatures between 160 and 200°C (Fig. 11A). Their ice-melting temperatures (T_m) vary widely from −21.2 to −8.1°C, and calculated salinities of the fluids from which the dolomite formed are in the range from 11.8 to 23.2 eq. wt. % NaCl (*Bodnar, 1993*) (Table 3; Fig. 11C). The coarse dolomite cement contained no workable primary inclusions, probably because of dissolution and recrystallization, which removed the inclusions in the weakest parts of crystal. For this reason, no coarse dolomite could be analyzed for their inclusions.

Natrolite, which occurs in association with dolomite, is also suitable for microthermometric studies. Primary inclusions in natrolite are relatively large (8 to 20 µm) and have regular and elongated shapes (Fig. 10B). Natrolite inclusions have rather higher homogenization temperatures (T_h from 232 to 351°C; Table 3; Fig. 11B) and their ice-melting temperatures range from −25.2 to −16.9°C, suggesting a salinity of 19.8 to 25.7 eq. wt. % NaCl (Table 3; Fig. 11C). Thus both homogenization temperatures and salinity of the fluids precipitating the natrolite appear to be distinctly higher than those from which the dolomite formed.

DISCUSSION

Four main types of dolomite were recognized in the Tengger Formation: Fd1 dolomites form a matrix that supports synchronously deposited white scattered grains of natrolite, analcine and Fe-bearing magnesite; massive or laminated Fd2 dolomites without synchronously deposited grains; Md dolomites are limited to laminae and bands which exhibit deformation structures; Cd dolomites are restricted to fracture infills. This study considers the Tengger Formation dolomites as primary products of direct precipitation during sedimentary and/or penecontemporaneous stages from hydrothermal fluids. These fluids have supplied magnesium for dolomite generation (e.g. *Last and Deckker, 1990*) and resulted in their high iron content.

Genetic model for syn-sedimentary hydrothermal dolomites

It is proposed that the input of hydrothermal fluids associated with volcanism at the base of the lake were synchronous with deposition and could have altered physical and chemical conditions sufficiently to facilitate the deposition of dolomites. The geochemical potential of hydrothermal fluids to form fault-related dolomites in the subsurface has been previously demonstrated, for example by *Nader et al. (2004)* and *Eickmann et al. (2009)*. In the Baiyinchagan Sag, such hydrothermal fluids discharged from faults and fractures into the bottom of the lake would have resulted in mixing with lake water in the presence of unconsolidated normal lacustrine terrigenous sediments. This mixing, together with a decrease in pressure and temperature of the hydrothermal fluid, would have driven the sequential precipitation of the various dolomites and associated minerals, forming the deposits observed in the cores. These dolomites should be called hydrothermal, because they apparently formed at higher than ambient temperature (*Machel and Lonnee, 2002*).

The vertical alternation between dolomite and mudstone/siltstone suggests that the hydrothermal fluid was introduced into the lake in pulses, with active hydrothermal phases alternating with periods of reduced activity or cessation of hydrothermal discharge. The lateral distribution of dolomites (Fig. 2) suggests rapid decay in precipitation potential with distance from the source of hydrothermal fluids (e.g. *Dekov et al., 2014; Lopez et al., 2017*). Firstly, the onset of hydrothermal activity was marked by formation of laminae or bands of Md dolomites intercalated with unconsolidated lacustrine sediments layers, giving way up-section to deposition of intermixed muds/silts and Md dolomites. The resulting localized buildup of dolomites associated with discharge of hydrothermal fluid resulted in syn-sedimentary deformation and folding, even syn-depositional brecciation of a number of earlier consolidated rocks such as white laminae and bands, with either local redeposited or transport over a short distance. This would have been followed by a period increased input of hydrothermal fluid, leading to greater upwelling and mixing within the lake. Local to the hydrothermal vents, highly idiomorphic natrolite, analcime, pyrite and/or dolomite and magnesite precipitated, within distinctly shaped grains. More distal from the vents, mixing of hydrothermal fluids with a higher fraction of lake water resulted in Fd1 and Fd2 dolomites and very fine analcime and natrolite precipitates inter-mixed with sediments redeposited in the lake sourced from the surrounding basin. Subsequently, during periods when hydrothermal discharge ceased, normal lacustrine mudstones and/or siltstone deposits accumulated, and no dolomites were formed. Thus, the hydrothermal fluids supplied the basic components for the formation of dolomites, and the lake served as a depositional environment for these components (in the form of the different dolomites, natrolite, analcime and magnesite). The dolomites of the Tengger Formation formed under the influence of both hydrothermal fluids and lake water, and can best be referred to as syn-sedimentary hydrothermal dolomites. This system may have been comparable to subaqueous exhalative systems thought to have formed carbonate chimneys in alkaline lakes of Afar (e.g. *Dekov, et al., 2014*) and at depth of more than 600 m in the South China Sea (*Sun et al., 2015*).

Evidence in support of syn-sedimentary hydrothermal dolomite formation

The proposed model of syn-sedimentary hydrothermal dolomites is supported by four separate lines of evidence: the large-scale tectonic and depositional environment, the petrography and occurrence of dolomites, associated minerals, and dolomite geochemical composition.

Tectonic and depositional setting

Continental rifting generated a lake basin within which muddy sediments accumulated, with a series of basin-bounding normal faults along which hydrothermal fluid circulated. Although there was little apparent volcanism in the Baiyinchagan Sag during the Early Cretaceous, abundant andesite, rhyolite, and pyroclastic rock was produced in the eastern part of the Erlian Basin (e.g., the Honghaoershute and Saihantala sags; *Lu et al., 2011; Ji et al., 2012; Li et al., 2014*). This suggests that the study area was under the indirect influence of volcanism. The extensional tectonics and volcanic activity gave rise to an abnormally high local geothermal gradient of *ca* 83°C.km^{-1} in the Baiyinchagan Sag (*Liu and Zhang, 2011*), significantly steeper than the current geothermal gradient of *ca* 35°C.km^{-1} (*Ren, 1998; Zhao et al., 2001*). The proximity of the dolomite to the fault zones suggests that the complex network of faults and fractures acted as conduits for migration of hydrothermal fluids (Fig. 2). The active tectonic regime and high heat flux would have both enhanced the permeability of fault/fracture network and provided a drive for convection of hydrothermal fluids (*Nader et al., 2004; Hollis et al., 2017*). The very high fluid temperature (≥300 ^{o}C) would be both thermodynamically and kinetically favourable for dolomite generation.

Dolomite texture, structure and composition

The contrasting textures and the high iron content of the different types of dolomite provide direct evidence for formation from hydrothermal fluids, and associated sedimentary structures point clearly to a primary origin.

Fd1 and Fd2 dolomites are microcrystalline (2 to 10 µm) and occur as non-planar to planar-subhedral crystals. This indicates that nucleation rate is higher than growth rate, which is characteristic of a high density of nucleation sites in a substrate and/or formation at relatively low temperature (<50 to 100℃) (*Gregg and Sibley, 1984*). Conditions commensurate with rapid-precipitation of fine-crystalline dolomite, such as high dolomite supersaturation and presence of precursor carbonates, are generally viewed as occurring in near-surface evaporative and/or shallow-burial environments (*Hips et al., 2015; Lu et al., 2015; Hou et al., 2016*). However, the co-occurrence of siliciclastic lacustrine sediments, and the apparent absence of $CaCO_3$ or abundant evaporites (e.g., gypsum or anhydrite), suggest the fine-crystalline dolomites are primary chemical precipitates penecontemporaneous with deposition of the lacustrine sediments. In addition, fine-crystalline dolomites in near-surface or shallow-burial environments tend to have a low (<2%) iron content, whether formed from marine (e.g. *Azomani et al., 2013; Olanipekun et al., 2014*) or lacustrine water (e.g. *Last et al., 2012*), whereas those in the Tengger Formation show significantly higher FeO content (>7%) (Table 1; Fig. 7B). This provides clear evidence that the Fd dolomites were not formed simply from lake water, but also involved hydrothermal fluid that was enriched in iron.

The interfaces between the Md and Fd dolomites and the lacustrine sediments are sharp, with no evidence of recrystallization of Fd dolomite or patchy replacement. Furthermore, there is an absence of replacement textures, such as submicron calcite domains in the dolomite. Texturally, Md dolomites display crystalline aggregates composed of subhedral to euhedral crystals, which indicates multiple growth episodes of the crystals (*Rosen and Coshell, 1992*). Md dolomites are also non-cathodoluminescent and show no zonation, possibly due to slower crystallization from a stable and homogeneous fluid (*Machel, 2004*). Laminae and bands of Md dolomites exhibit deformation structures and brecciation, indicating a syn-sedimentary origin rather than formation during later diagenesis. The lower FeO content (mean 4.5%) compared to the fine-crystalline dolomites (Table 1; Fig. 7B), may be result from the removal of iron from the fluid via the growth of cubic pyrite.

Cd dolomites are a later stage fracture infill, and are characterized by large crystal sizes and undulatory extinction. The undulatory extinction is indicative of crystal growth at high temperatures (>60 °C) responsible for distorted crystal lattices (*Warren, 2000*). Compositionally the Cd dolomites are similar to the Fd dolomites, suggesting precipitation either from similar fluids, or at different evolutionary stages of the same fluid (*Boni et al. 2000; Warren, 2000*).

Significance of associated minerals

All dolomites are associated with unusual and distinctive minerals which provide further evidence for high temperature precipitation. White grains of natrolite and analcime occur evenly mixed with Fd1 dolomite, or replaced by Md dolomite in the white laminae/bands. Natrolite and analcime are commonly euhedral, relatively large (up to 200 μm) crystals, without remnant precursors, and display consistent chemical compositions (Table 1). This mineral assemblage is interpreted to have precipitated from hydrothermal fluids in response to changing temperature or other physicochemical conditions, rather than by replacement within a burial environment that would typically produce single-component minerals such as siliceous minerals (*Liu et al., 2010*).

Fluid inclusions in the natrolite have high homogenization temperatures of 232 to 351°C, with salinity from 19.8 to 25.7 eq. NaCl wt. %, indicating formation from a high-salinity hydrothermal fluid. *Ghobarkar and Schäf* (*1999*) and *Kumar and Chattopadhyaya* (*2006*) verified under laboratory conditions that natrolite and analcime could directly precipitate from a hydrothermal fluid to produce euhedral crystals, and suggest the crystallizing temperature for analcime is ~50°C higher than that for natrolite. Similarly, magnesite associated with dolomite has been reported to have formed from hydrothermal fluids at high temperatures (>180°C, *Herrero et al., 2011*; <500°C**,** *Hurai et al., 2011*). The cubic form of the pyrite within the dolomite provides further support for formation in a high-temperature environment (Fig. 5H and I). Cubic pyrite has been reported to form at temperatures up to 250 to 300℃ (*Murowchick and Barnes, 1987; Kouzmanov et al., 2002*), but at > 450ºC pyrite forms octahedron and pentagonal dodecahedron crystals (*Cai and Zhou, 1993; Graham and Ohmoto, 1994*). The higher temperature and salinity of fluids forming the natrolite, relative to that of the Md dolomites (Fig. 11C), implies changes in hydrothermal fluid from which the minerals precipitated. It is proposed that the hydrothermal fluids evolved along a pathway that started with the formation of zeolite, which requires higher temperature and salinity, and consumed Na-Al-Si.

Cooling of the residual fluids, that were relatively enriched in Fe-Mg-Ca, favoured precipitation of Fe-bearing magnesite and dolomite. Although this would result in a small reduction in the total dissolved solids, the significant reduction in salinity indicated by the fluid inclusion data (from 19.8 to 25.7 eq. wt. % NaCl in the natrolite to 11.8 to 23.2 eq. wt. % NaCl in the medium-crystalline dolomite; Fig.11C) suggests that the cooling hydrothermal fluids also mixed with and were diluted by lower salinity lake water. Similar processes are inferred to result in formation of the fine-crystalline dolomite and zeolite which were then mixed with terrigenous sediments, although the fine texture means that changes in the precipitation path cannot be directly observed.

Implications of isotopes and REEs

The isotopic composition of the Fd1, Md and Cd dolomites (Fig. 8) is comparable to that of previously described subsurface hydrothermal dolomites (e.g. *Herrero et al., 2011; Haeri-Ardakani et al., 2013*), whereas the Fd2 dolomites are notably heavier, especially in oxygen. Isotopic values of Fd1 and Fd2 dolomite are distinct from those of dolomite cements in the mudstone (Fig. 8) There is little isotopic fractionation of $^{13}C/^{12}C$ with temperature, and thus the $\delta^{13}C$ value of the dolomite reflects that of the parent fluids (*Tucker and Wright, 1990*). Whilst texturally distinct, the $\delta^{13}C$ of most of the different dolomites in the study area lie within the range +2‰ to +4‰, with the exception of some Fd2 dolomites with heavier $\delta^{13}C$. The latter are interpreted to result from abundant degassing of light CO_2 from ascending hydrothermal fluids reflecting a pressure reduction (*Kele et al., 2008*). The $\delta^{18}O$ values of the dolomites reflect both the temperature and the composition of the parent fluids, suggesting that precipitation takes place under isotopic equilibrium (*Matthews and Katz, 1977; Horita, 2014*). Many high-temperature hydrothermal dolomites are interpreted to form from fluids with negative $\delta^{18}O$ values (Fig. 8) (*Boni et al., 2000; Gasparrinia et al., 2006; Martín-Martín et al., 2015; Hou et al., 2016*).

Given the formation temperature of Md dolomites from fluid inclusions (T_h=167 to 283°C), the method of *Land* (*1983*) is used to calculate the fractionation factor between the dolomite and the parent fluids. This suggests $\delta^{18}O$ values of the parent fluid of +3 to +4‰ SMOW, and formation of texturally distinct dolomites from fluids at different temperatures. The highest temperature of formation is for the Cd dolomite (~182 to 221°C), with the Fd1 dolomite formed at temperatures (~141 to 282°C) that were significantly higher than the Fd2 dolomites (~81 to 124°C). The variations in the calculated formation temperatures could be explained by changes in the ratio of lake water (mean annual temperature about 20°C; *Chen, 2010*) mixing with hot hydrothermal fluids that ascended rapidly from depth. The progressive decrease in $\delta^{18}O$ values is consistent with that observed in hydrothermal carbonate chimneys (*Eickmann, et al., 2009; Dekov, et al., 2014*), in which different carbonate minerals formed in evolved hydrothermal fluids.

The detailed mixing process of hydrothermal fluids also can be revealed by the REEs in the Tengger Formation dolomites. The total REE (ΣREE) content of the dolomites are far higher than those of dolomites of evaporative, reflux, or burial origin (which typically do not exceed 100 ppm; e.g. *Haeri-Ardakani et al., 2013; Liu et al., 2017*) and most samples ΣREE contents are within the range reported for hydrothermal dolomites (30 to 300 ppm) (*Kučera et al., 2009*). The Cd dolomites that are interpreted to have precipitated from hydrothermal fluids to infill fractures exhibit compositions close to a hydrothermal end-member and are characterized by the lowest ΣREE content of all the dolomites (Fig. 9C). The higher ΣREE contents of the other Tengger Formation dolomites, and the shape of their REE_N profiles, suggest there was an enhanced influx of REEs. Michard (*1989*) suggested that a decrease in fluid pH may increase ΣREE content, and laboratory experiments (Pourret et al., *2007*) demonstrated that enhanced alkalinity can lead to HREE enrichment. Thus hydrothermal fluids with higher alkalinity could have produced the Md dolomites, resulting in more pronounced HREE enrichment (Fig. 9B). Increased mixing with lake water would decrease the pH of the hydrothermal fluid, accounting for the higher ΣREE of Md dolomites. The pH and alkalinity would continue to decrease as the fraction of lake water increased, resulting in precipitation of Fd1 and Fd2 dolomites with higher REE contents and greater HREE depletion (Fig. 9A). There may also be a REE contribution from the non-carbonate fraction, such as siliciclastics which make up more than 5% of the deposits and are typically REE-rich (*Banner et al., 1988*). The association of Fd1 and Fd2 dolomites with normal lacustrine sediments (feldspars and clays) may also contribute to their relatively higher ΣREE content. Moreover, all dolomites show similar Eu and Ce anomalies, indicating formation under stable redox conditions, such as would be expected with deposition in a deep lake. The Fd1, Fd2 and Md dolomites could have inherited a positive Tb and negative Dy anomaly from a hydrothermal fluid, and a positive Yb anomaly from lake water, because the chemical features of other REEs change systematically along the REE series of parent fluids rather than environment (*Sholkovitz and Shen, 1995*).

The supporting evidence above provides clear evidence that the dolomites of the Tengger Formation formed under the influence of both hydrothermal fluids and lake water, with the different dolomite types reflecting different degrees of mixing between two fluids. Theses dolomites thus show important differences from those found in the Tarim and Sichuan basins that appear to have result from alteration of limestone by hydrothermal fluids. The latter are identified as products of a replacement reaction based on preservation of depositional textures and development of zebra and brecciated textures, none of which are seen in the Tengger Formation dolomites, as well as geochemical features inherited from the precursor limestone (e.g. *Dong et al., 2016; Feng et al., 2017*).

CONCLUSIONS

Based on petrographic features, elemental composition, oxygen and carbon isotopic composition, REE contents and fluid inclusion properties, the following conclusions are drawn about the Tengger Formation dolomites in the Baiyinchagan Sag of the Earlian Basin.

1 Four different types of dolomite can be recognized: fine-crystalline dolomite present either as white matrix-supporting grains (Fd1) or as dolomitic mudstone (Fd2); medium-crystalline dolomite (Md) composed of white laminae and bands; and rare coarse dolomite (Cd) occurring as saddle dolomite filling fractures. Importantly, dolomites are mixed or interbedded with lacustrine terrestrial sediments, suggesting synchronous deposition, and co-occur with natrolite, analcime, Fe-bearing magnesite, pyrite and barite.

2 The fine-crystalline dolomites (Fd1 and Fd2) have a similar geochemical composition to the Cd dolomite in terms of a high FeO content, while the Md dolomites have the highest CaO and MgO contents and lowest FeO contents. This demonstrates that the Tengger Formation dolomites must have formed under the influence of Fe-rich and Mg-rich hydrothermal fluids.

3 The Md dolomites precipitated at high temperatures from hydrothermal fluids that mixed with a relatively minor amount of lake water local to the vents, that may thus have had a higher alkalinity than the fluids that formed the Fd dolomites. As the hydrothermal plume expanded within the lake the fluids would have retained a relatively high but decreased alkalinity, producing the Fd1 dolomites accompanied by white grains. Mixing of increasing amounts of lake water with the hydrothermal fluid, would have reduced temperatures still further and precipitated the Fd2 dolomites. At a later stage high temperature Cd dolomite precipitated locally to fill fractures.

4 A combination of the geological setting and the petrography and geochemistry of the dolomites, suggests strong localized discharge of very high-temperature saline-alkaline hydrothermal fluids through boundary faults and accompanying fractures, under an abnormally high heat flux. This hydrothermal fluid mixed with cold lake water, creating conditions favourable to the precipitation of dolomite and associated minerals. The chemical and physical processes that lead to accumulation of the Tengger Formation thus reflect both hydrothermal and sedimentary processes. The hydrothermal fluids would have supplied the basic chemical components for formation of the dolomites, while the lake water moderated the composition and temperature of the hydrothermal fluid and served as a depositional environment.

ACKNOWLEDGEMENTS

We are grateful to the staff from Zhongyuan oil field for kind assistance in collection of core samples, and others who are helpful for laboratory work. We thank the anonymous reviewers and Associate Editor Cathy Hollis for constructive and thoughtful comments that helped improved the manuscript. This study was supported under grants from the National Science Foundation of China (Grant No. 41472094, 41502099).

REFERENCES

Azomani, E., Azmy, K., Blamey, N., Brand, U. and **Al-Aasm, I.** (2013) Origin of Lower Ordovician dolomites in eastern Laurentia: Controls on porosity and implications from geochemistry. *Mar. Petrol. Geol*., 40, 99-114.

Banner, J.L., Hanson, G.N. and **Meyers, W.J.** (1988) Rare earth element and Nd isotopic variations in regionally extensive dolomites from the Burlington-Keokuk formation (Mississippian): implications for REE mobility during carbonate diagenesis. *J. Sediment. Petrol*., 58, 415-432.

Barnes, I. and **O'Neil, J.R.** (1971) Calcium-magnesium carbonate solid solutions from Holocene conglomerate cements and travertines in the Coast Range of California. *Geochim. Cosmochim.*

Acta., 35, 699-718.

Bau, M., Koschinsky, A., Dulski, P. and **Hein, J.R.** (1996) Comparison of the partitioning behaviours of yttrium, rare earth elements, and titanium between hydrogenetic marine ferromanganese crusts and seawater, *Geochim. Cosmochim. Acta.*, 60, 1709-1725.

Bodnar, R.J. (1993) Revised equation and table for determining the freezing point depression of H_2O-NaCl solutions. *Geochim. Cosmochim. Acta*., 57, 683-684.

Boni, M., Parente, G., Bechstädt, T., Vivo, B.D. and **Iannace, A.** (2000) Hydrothermal dolomites in SW Sardinia (Italy): Evidence for a widespread late-Variscan fluid flow event. *Sediment. Geol*., 131, 181-200.

Bontognali, T. R., Vasconcelos, C., Warthmann, R.J., Bernascon, S. M., Dupraz, C., Strohmenger, C. J. and **McKenzie, J. A.** (2010) Dolomite formation within microbial mats in the coastal sabkha of Abu Dhabi (United Arab Emirates). *Sedimentology*, 57, 824-844.

Cai, Y. and **Zhou, M.** (1993) Experiental study on the characteristics of pyrite crystal form in gold deposit. *Sci. China, Ser. B*, 23, 972-978 (in Chinese).

Chen, D. (2010) The lacustrine carbonate and their sedimentary environment of early Cretaceous Yixian Formation in western Liaoning. PhD Thesis, Northeastern Univ., Shenyang, 102-105. (in Chinese with English abstract).

Dekov, V. M., Egueh, N. M., Kamenov, G. D., Bayon, G., Lalonde, S. V., Schmidt, M., Liebetrau, V., Munnik, F., Fouquet, Y., Tanimizu, M., Awaleh, M.O., Guirreh, I. and **Le Gall, B.** (2014) Hydrothermal carbonate chimneys from a continental rift (Afar Rift): Mineralogy, geochemistry, and mode of formation. *Chem Geol*., 387, 87-100.

Deng, S., Dong, H., Lv, G., Jiang, H., Yu, B. and **Bishop, M.E.** (2010) Microbial dolomite precipitation using sulfate reducing and halophilic bacteria: results from Qinghai Lake, Tibetan Plateau, NW China. *Chem. Geol.*, 278, 151-159.

Deng, Y.X. (2006) Structural analysis and reservoir character in Baiyinchagan Depression. PhD Thesis, China Univ. Geosci., Beijing, 21-23. (in Chinese with English abstract).

Dickson, J.A.D. (1966) Carbonate identification and genesis as revealed by staining. *J. Sediment. Petrol*. 36, 491-505.

Dong, S., Chen, D., Zhou, X., Qian, Y., Tian, M. and **Qing, H.** (2016) Tectonically driven dolomitization of Cambrian to Lower Ordovician carbonates of the Quruqtagh area, north-eastern flank of Tarim Basin, north-west China. *Sedimentology*, 64, 1079-1106.

Dou, L., Zhu, Y., Yang, T., Xu, S. and **Ping, X.** (1998) Origins of heavy oils in the Erlian Basin, NE China. *Mar. Pet. Geol.*, 15, 769-781.

Eickmann, B., Bach, W., Rosner, M. and **Peckmann, J.** (2009) Geochemical constraints on the modes of carbonate precipitation in peridotites from the Logatchev hydrothermal vent field and Gakkel ridge. *Chem. Geol.*, 268, 97-106.

Feng, M., Wu, P., Qiang, Z., Liu, X., Duan, Y. and **Xia, M.** (2017) Hydrothermal dolomite reservoir in the Precambrian Dengying Formation of central Sichuan Basin, southwestern China. *Mar. Pet. Geol.*, 82, 206-219.

Gasparrinia, M., Bechstadta, T. and **Bonib, M.** (2006) Massive Hydrothermal Dolomites in the Southwestern Cantabrian Zone (Spain) and their relation to the Late Variscan evolution. *Mar. Pet. Geol.*, 23, 543-568.

Ghobarkar, H. and **Schäf, O.** (1999) Effect of temperature on hydrothermal synthesis of analcime and viséite. *Mater. Sci. Eng., B.*, 60, 163-167.

Gregg, J.M. and **Sibley, D.F.** (1984) Epigenetic dolomitization and the origin of xenotopic dolomite texture. *J. Sediment. Res.*, 54, 908–931.

Gregg, J. M., **Bish, D. L.**, **Kaczmarek, S. E.** and **Machel, H. G.** (2015) Mineralogy, nucleation and growth of dolomite in the laboratory and sedimentary environment: A review. *Sedimentology*, 62, 1749-1769.

Gromet, L.P., Haskin, L.A., Korotev, R.L. and **Dymek, R.F.** (1985) The "North American shale composite": its compilation, major and trace element characteristics. *Geochim. Cosmochim. Acta.*, 48, 2469-2482.

Guo, Q., Zhong, D., Zhang, F., Liu, X., Fang, L. and **Li, J.** (2012) Origin of the Lower Cretaceous Lacustrine dolostones in Baiyinchagan Sag of Erlian Basin, Inner Mongolia. *J. Palaeogeogr.*, 14, 59-68. (in Chinese with English abstract).

Guo, Q., Li, Z., Qin, M., Zhong, D., Zhang, F., Jia, C. and **Wu, J.** (2014) Discussion of hydrothermal sedimentary sequence in Baiyinchagan Sag of Erlian Basin, Inner Mongolia. *Acta Sedimentol. Sinica*, 32, 809-815. (in Chinese with English abstract).

Haeri-Ardakani, O., Al-Aasm, I. and **Coniglio, M.** (2013) Petrologic and geochemical attributes of fracture-related dolomitization in Ordovician carbonates and their spatial distribution in southwestern Ontario, Canada. *Mar. Pet. Geol.*, 43, 409-422.

Hendry, J.P., Gregg, J.M., Shelton, K.L., Somerville, I.D. and **Crowley, S.F.** (2015) Origin, characteristics and distribution of fault-related and fracture-related dolomitization: insights from Mississippian carbonates, Isle of Man. *Sedimentology*, 62, 717-752.

Herrero, M.J., Martín-Pérez, A., Alonso-Zarza, A.M., Gil-Peña, I., Meléndez, A. and **Martín-García, R.** (2011) Petrography and geochemistry of the magnesites and dolostones of the Ediacaran Ibor Group (635 to 542 Ma), western Spain: Evidences of their hydrothermal origin. *Sediment. Geol.*, 240, 71-84.

Hips, K., Haas, J., Poros, Z., Kele, S. and **Budai, T.** (2015) Dolomitization of Triassic microbial mat deposits (Hungary): origin of microcrystalline dolomite. *Sediment. Geol.*, 318, 113-129.

Hollis, C., Bastesen, E., Boyce, A., Corlett, H., Gawthorpe, R., Hirani, J. and **Rotevatn, A.** (2017) Fault-controlled dolomitization in a rift basin. *Geology*, 45, 219-222.

Horita, J. (2014) Oxygen and carbon isotope fractionation in the system dolomite-water-CO_2, to elevated temperatures. *Geochim. Cosmochim. Acta*, 129, 111-124.

Hou, Y., Azmy, K., Berra, F., Jadoul, F., Blamey, N.J.F., Gleeson, S.A. and **Brand, U.** (2016) Origin of the Breno and Esino dolomites in the western Southern Alps (Italy): Implications for a volcanic influence. *Mar. Pet. Geol.*, 69, 38-52.

Huang, H., Jin, G., Lin, C. and **Zheng, Y.** (2003) Origin of an unusual heavy oil from the Baiyinchagan Depression, Erlian basin, northern China. *Mar. Pet. Geol.*, 20, 1-12.

Hurai, V., Huraiová, M., Koděra, P., Prochaska, W., Vozárová, A. and **Dianiška, I.** (2011). Fluid inclusion and stable CO isotope constraints on the origin of metasomatic magnesite deposits of the Western Carpathians, Slovakia. *Russ. Geol. Geophys.*, 52, 1474-1490.

Ji, H., Yang, D., Gao, X., Fang, X. and **Wang, W.** (2012) Characteristic of Mesozoic volcanic rock and analysis of reservoir controlling factors in the Honghaoershute Sag of Erlian Basin. *Acta Geol. Sin.*, 86, 1227-1240. (in Chinese with English abstract).

Jiao, X., Liu, Y., Yang, W., Zhou, D., Li, H., Nan, Y. and **Jin, M.** (2018) A magmatic-hydrothermal lacustrine exhalite from the Permian Lucaogou Formation, Santanghu Basin, NW China–The volcanogenic origin of fine-grained clastic sedimentary rocks. *J. Asian Earth Sci.*, 156, 11-25.

Jones, G. D., **Whitaker, F. F.**, **Smart, P. L.** and **Sanford, W. E.** (2004). Numerical analysis of seawater circulation in carbonate platforms: II. The dynamic interaction between geothermal and brine reflux circulation. *Am. J. Sci.*, 304, 250-284.

Kaufman, J., Hanson, G.N. and **Meyers, W.J.** (1991) Dolomitization of the Devonian Swan Hills Formation, Rosevear Field, Alberta, Canada. *Sedimentology*, 38, 41-66.

Kele, S., **Demény, A., Siklósy, Z., Németh, T., Tóth, M.** and **Kovács, M.B.** (2008) Chemical and stable isotope composition of recent hot-water travertines and associated thermal waters, from Egerszalók, Hungary: Depositional facies and non-equilibrium fractionation. *Sediment. Geol.*, 211, 53-72.

Kouzmanov, K., Bailly, L., Ramboz, C., Rouer, O. and **Beny, J. M.** (2002) Morphology, origin and infrared microthermometry of fluid inclusions in pyrite from the Radka epithermal copper deposit, Srednogorie zone, Bulgaria. *Miner. Depos.*, 37, 599-613.

Kučera, J., Cempírek, J., Dolníček, Z., Muchez, P. and **Prochaska, W.** (2009) Rare earth elements and yttrium geochemistry of dolomite from post-Variscan vein-type mineralization of the Nízký Jeseník and Upper Silesian Basins, Czech Republic. *J. Geochem. Explor.*, 103, 69-79.

Kumar, S. and **Chattopadhyaya, M.C.** (2006) Synthesis of natrolite using the hydrothermal apparatus. *J. Indian Chem. Soc.*, 83, 1288-1290.

Land, L.S. (1983) The application of stable isotopes to studies of the origin of dolomite and to problems of diagenesis of clastic sediments. In: *Stable Isotopes in Sedimentary Geology* (Eds M.A. Arthur and T.F. Anderson) *Soc.Econ.Paleont. Miner. Short Course*, 10, 4.1-4.22.

Lapponi, F., Bechstädt, T., Boni, M., Banks, D.A. and **Schneider, J.** (2014) Hydrothermal dolomitization in a complex geodynamic setting (Lower Palaeozoic, northern Spain). *Sedimentology*, 61, 411-443.

Last, F.M., Last, W.M. and **Halden, N.M.** (2012) Modern and Late Holocene dolomite formation: Manito lake, Saskatchewan, Canada. *Sediment. Geol.*, 281, 222-237.

Last, W.M. and **Deckker, P.D.** (1990) Modern and Holocene carbonate sedimentology of two saline volcanic maar lakes, southern Australia. *Sedimentology*, 37, 967-981.

Lavoie, D. and **Chi, G.** (2010) Lower Paleozoic foreland basins in eastern Canada: tectono-thermal events recorded by faults, fluid and hydrothermal dolomites. *Bull. Can. Petrol. Geol.*, 58, 17-35.

Leach, D.L. and **Sangster, D.F.** (1993) Mississippi Valley-type lead-zinc deposits. In: *Mineral Deposit Modeling* (Eds R.V. Kirkham, J.M. Duke, W.D. Sinclair and R.I. Thorpe) *Geol. Ass. Canada Spec. Paper*, 40, 289-314.

Li, H., Liu, Y., Liang, H., Luo, Q., Li, W., Zhou, X., Jiao, X., Yang, R., Lei, C. and **Sun, Q.** (2012a) Lithology and origin analysis of sublacustrine hydrothermal deposits characterized by analcime, Sanidine, Dolomite, Quartz, etc. in Lucaogou formation, Middle Permian, Santanghu Basin, Northeast Xinjiang, China. *Acta Sedimentol. Sinica*, 30, 205-218. (in Chinese with English abstract).

Li, H., Liu, Y., Liang, H., Zhou, X., Jiao, X., Liu, H., Yang, R. and **Lei, C.** (2012b) Origin of lacustrine dolostones of the Middle Permian Lucaogou Formation in Santanghu Basin of Xinjiang. *J. Palaeogeogr.*, 14, 45-58. (in Chinese with English abstract).

Li, H., Shen, K., Nie, F., Kuang, W. and **He, D.** (2012) Sedimentary Evolution in Meso-Cenozoic and Uranium Mineralization of Erlian Basin. *J. East China Inst. Technol.* (Natural Science), 35, 301-308. (in Chinese with English abstract).

Li, H., Gao, X., Yang, D., Zhu, C., Wei, Q. and **Zhang, L.** (2014) Characteristics and distribution prediction of Cretaceous volcanic reservoirs in Saihantala Sag, Erlian Basin. *Petro. Geol. Exper.*, 36, 442-449. (in Chinese with English abstract).

Liu, C., Xie, Q., Wang, G., He, W., Song, Y., Tang, Y. and **Wang, Y.** (2017) Rare earth element characteristics of the carboniferous Huanglong formation dolomites in eastern Sichuan basin, southwest china: Implications for origins of dolomitizing and diagenetic fluids. *Mar. Petrol. Geol.*, 81, 33-49.

Liu, C. and **Zhang, X.** (2011) Relationship between paleogeothermal and hydrocarbon generation in the Baiyinchagan Depression, Erlian Basin: *J. Shandong Univ. Sci. Tech.*, 30, 12-19. (in Chinese with English abstract).

Liu, W., Huang, Y., Pang, Y. and **Wang, P.** (2010) Diagenesis of intermediate and mafic volcanic rocks of Yingcheng Formation (K1y) in the Songliao basin: Sequential crystallization, amygdule filling and reservoir effect. *Acta Petrologica Sinica*, 21, 158-164. (in Chinese with English abstract).

Liu, Y., Li, H., Zhu, Y., Hu, T., Fu, G., Liu, H., Zhou, X. H., Zheng, C. and **Fan, T.** (2010) Permian lacustrine eruptive hydrothermal dolomites, Santanghu Basin, Xinjiang Province. *Acta Sedimentol. Sinica*., 28, 861-867. (in Chinese with English abstract).

Liu, Y., Jiao, X., Li, H., Yuan, M., Yang, W., Zhou, X., Liang, H., Zhou, D, Zheng, C., Sun, Q. and **Wang, S.** (2011) Primary dolostone formation related to mantle-originated exhalative hydrothermal activities, Permian Yuejingou section, Santanghu area, Xinjiang, NW *China. Sci. China Earth. Sci*., 41, 1862-1871. (in Chinese with English abstract).

Lonnee, J. and **Machel, H.G.** (2006) Pervasive dolomitization with subsequent hydrothermal alteration in the Clarke Lake gas field, Middle Devonian Slave Point Formation, British Columbia, *Canada. AAPG Bull*., 90, 1739-1761.

Lopez, B., Camoin, G., Özkul, M., Swennen, R. and **Virgone, A.** (2017) Sedimentology of coexisting travertine and tufa deposits in a mounded geothermal spring carbonate system, Obruktepe, Turkey. *Sedimentology*, 64, 903-931.

Lu, Z., Na, R., Cui, J., Wang, Y. and **Yang, G.** (2011) Volcanic rock reservoir of the Cretaceous in Honghao'ershute Sag in Erlian Basin, Inner Mongolia. *J. Palaeogeogr*., 13, 201-208. (in Chinese with English abstract).

Lu, X., Shi, J., Zhang, S., Zou, N., Sun, G. and **Zhang, S.** (2015) The origin and formation model of Permian dolostones on the northwestern margin of Junggar Basin, China. *J. Asian Earth Sci.*, 105, 456-467.

Machel, H.G. (2004) Concepts and models of dolomitization: a critical reappraisal. In: *The Geometry and Petrogenesis of Dolomite Hydrocarbon Reservoirs* (Eds C.J.R. Braithwaite, G. Rizzi and G. Darke) *Geol. Soc. London Spec. Publ*., 235, 7-63.

Machel, H.G. and **Lonnee, J.** (2002) Hydrothermal dolomite-a product of poor definition and imagination. *Sediment. Geol.*, 152, 163-171.

Mansurbeg, H., Morad, D., Othman, R., Morad, S., Ceriani, A., Al-Aasm, I., Kolo, K., Spirov P., Proust, J.N., Preat, A. and **Koyi, H.** (2016) Hydrothermal dolomitization of the Bekhme formation (upper cretaceous), Zagros basin, Kurdistan Region of Iraq: Record of oil migration and degradation. *Sediment. Geol.*, 341, 147-162.

Martín-Martín, J.D., Gomez-Rivas, E., Bover-Arnal, T., Travé, A., Salas, R. and **Moreno-Bedmar, J.A.** (2013) The Upper Aptian to Lower Albian syn-rift carbonate succession of the southern Maestrat Basin (Spain): Facies architecture and fault-controlled stratabound dolostones. *Cretaceous Res.*, 41, 217-236.

Martín-Martín, J.D., Travé, A., Gomez-Rivas, E., Salas, R., Sizun, J.P., Vergés, J., Corbella, M., Stafford, S.L. and **Alfonso, P.** (2015) Fault-controlled and stratabound dolostones in the Late Aptian-earliest Albian Benassal Formation (Maestrat Basin, E Spain): Petrology and geochemistry constrains. *Mar. Pet. Geol.*, 65, 83-102.

Matthews, A. and **Katz, A.** (1977). Oxygen isotope fractionation during the dolomitization of calcium carbonate. *Geochim. Cosmochim. Acta*, 41, 1431-1438.

Michard, A. (1989) Rare earth element systematics in hydrothermal fluids. *Geochim. Cosmochim. Acta*, 53, 745-750.

Murowchick, J.B. and **Barnes, H.L.** (1987) Effects of temperature and degree of supersaturation on pyrite morphology. *Geochem. Trans.*, 1, 23-33.

Nader, F. H., Swennen, R. and **Ellam, R.** (2004) Reflux stratabound dolostone and hydrothermal volcanism-associated dolostone: a two-stage dolomitization model (Jurassic, Lebanon). *Sedimentology*, 51, 339-360.

Olanipekun, B., Azmy, K. and **Brand, U.** (2014) Dolomites of the Boat Harbour Formation in the Northern Peninsula, western Newfoundland, Canada: implications for dolomitization history and porosity control. *AAPG Bull.*, 98, 765-791.

Pourret, O., Davranche, M., Gruau, G. and **Dia, A.** (2007) Competition between humic acid and carbonates for rare earth elements complexation. *J. Colloid Interface Sci.*, 305, 25-31.

Ren, J., Li, S. and **Jiao, G.** (1998) Extensional tectonic system of Erlian Fault Basin Group and Its deep background. *Earth Sci. J. China Univ. Geosci.*, 23, 567-572. (in Chinese with English abstract).

Ren, Z. (1998) Comparative Research on Tectonical Thermal History of Sedimentary Basins in the North China. PhD Thesis, Northwest Univ., Xian, 64-67. (in Chinese with English abstract).

Rosen, M.R. and **Coshell, L.** (1992) A new location of Holocene dolomite formation, Lake Hayward, Western Australia. *Sedimentology*, 39, 161–166.

Selleck, B.W. (1978) Syndepositional brecciation in the Potsdam sandstone of northern New York State. *J. Sediment. Res.*, 48, 1177-1184.

Shepherd, T.J., Rankin, A.H. and **Alderton, D.H.M.** (1985) A Practical Guide to Fluid Inclusion Studies. *Blackie Academic and Professional, London, 224 pp.*

.

Sholkovitz, E. and **Shen, G.T.** (1995) The incorporation of rare earth elements in modern coral.

Geochim. Cosmochim. Acta., 59, 2749-2756.

Song, B., Han, H., Cui, X., Dong, X. and **Chen, J.** (2015) Petrogenesis analysis of lacustrine analcite dolostone of the Member 4 of Paleogene Shahejie Formation in Liaohe Depression, Bohai Bay Basin. *J. Palaeogeogr*., 17, 33-44. (in Chinese with English abstract).

Sun, Z., Wei, H., Zhang, X., Shang, L., Yin, X., Sun, Y., Xu, L., Huang, W. and **Zhang, X.** (2015) A unique Fe-rich carbonate chimney associated with cold seeps in the northern Okinawa trough, east china sea. *Deep-Sea ReS.,* Part I, 95, 37-53.

Tucker, M.E. and **Wright V.P.** (1990) Carbonate Sedimentology. *Blackwell Scientific Publication*, Palo Alto, 384 pp.

Vandeginste, V., Swennen, R., Allaeys, M., Ellam, R.M., Osadetz, K. and **Roure, F.** (2012) Challenges of structural diagenesis in foreland fold-and-thrust belts: a case study on paleofluid flow in the Canadian Rocky Mountains west of Calgary. *Mar. Pet. Geol*., 35, 235-251.

Wang, J. (2006) On the dynamic system of oil and gas migration and accumulation in Baiyinchagan depression.PhD Thesis,. China Univ. Geosci., Beijing, 11-18. (in Chinese with English Abstract).

Warren, J. (2000) Dolomite: occurrence, evolution and economically important associations. *Earth Sci. Rev*., 52, 1-81.

Wei, A., Xue, C., Xiang, K., Li, J., Liao, C. and **Akhter, Q.J.** (2015) The ore-forming process of the Maoping Pb-Zn deposit, northeastern Yunnan, China: Constraints from cathodoluminescence (CL) petrography of hydrothermal dolomite. *Ore Geol. Rev*., 70, 562-577.

Wen, H., Zheng, R., Qing, H., Fan, M., Li, Y. and **Gong, B.** (2014) Primary dolostone related to the Cretaceous lacustrine hydrothermal sedimentation in Qingxi Sag, Jiuquan Basin on the northern Tibetan Plateau. *Sci. China Earth. Sci*., 44, 591-604. (in Chinese with English abstract).

Whitaker, F. F. and **Smart, P. L.** (1993) Circulation of Saline Ground Water In Carbonate Platforms - A Review And Case Study From The Bahamas. In: *Diagenesis and Basin Development*)Eds A.D. Horbury and A.G., Robinson), AAPG Studies in Geology 36, 113-134.

Xiao, A. and **Yang, S.** (2001) Geodynamic Background on Formation of Erlian Basin. *Oil Gas Geol*., 22, 137-140. (in Chinese with English abstract).

Zhao, G., Zhang, J., Zhang, Y., Yan, D., Song, Z. and **Niu, X.** (2001) Characteristics and Pool-forming Regularity of Immature Oil in Western Baiyinchagan Depression, Erlian Basin. *Petrol. Explor. Dev*., 28, 4-7. (in Chinese with English abstract).

Zheng, R., Wen, H., Fan, M., Wang, M., Wu, G. and **Xia, P.** (2006) Lithological characteristics of sublacustrine white smoke type exhalative rock of the Xiagou Formation in Jiuxi Basin. *Acta Petrologica Sinica*, 22, 3028-3038. (in Chinese with English abstract).

Zhong, D., Jiang, Z., Guo, Q. and **Sun, H.** (2015) A review about research history, situation and prospects of hydrothermal sedimentation. *J. Palaeogeogr*., 17, 285-296. (in Chinese with English abstract).

Figure and captions

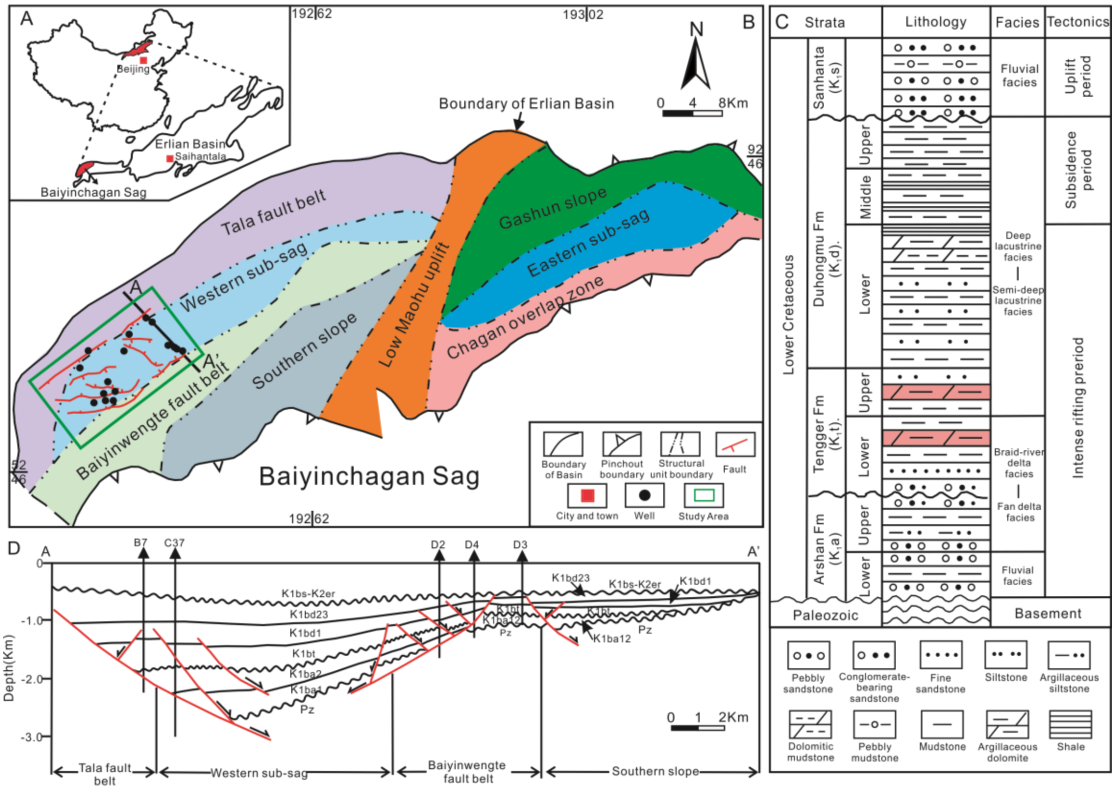

Fig. 1. (A) Location of the Baiyinchagan Sag in the Erlian Basin of northern China; (B) Simplified structure map of the Baiyinchagan Sag; (C) Detailed stratigraphic column of the Lower Cretaceous in Baiyinchagan (after drilling data of *Zhongyuan Oilfield, 2008*); (D) Structural cross section of a half-graben in the westernmost area of the basin (modified from *Wang, 2006*).

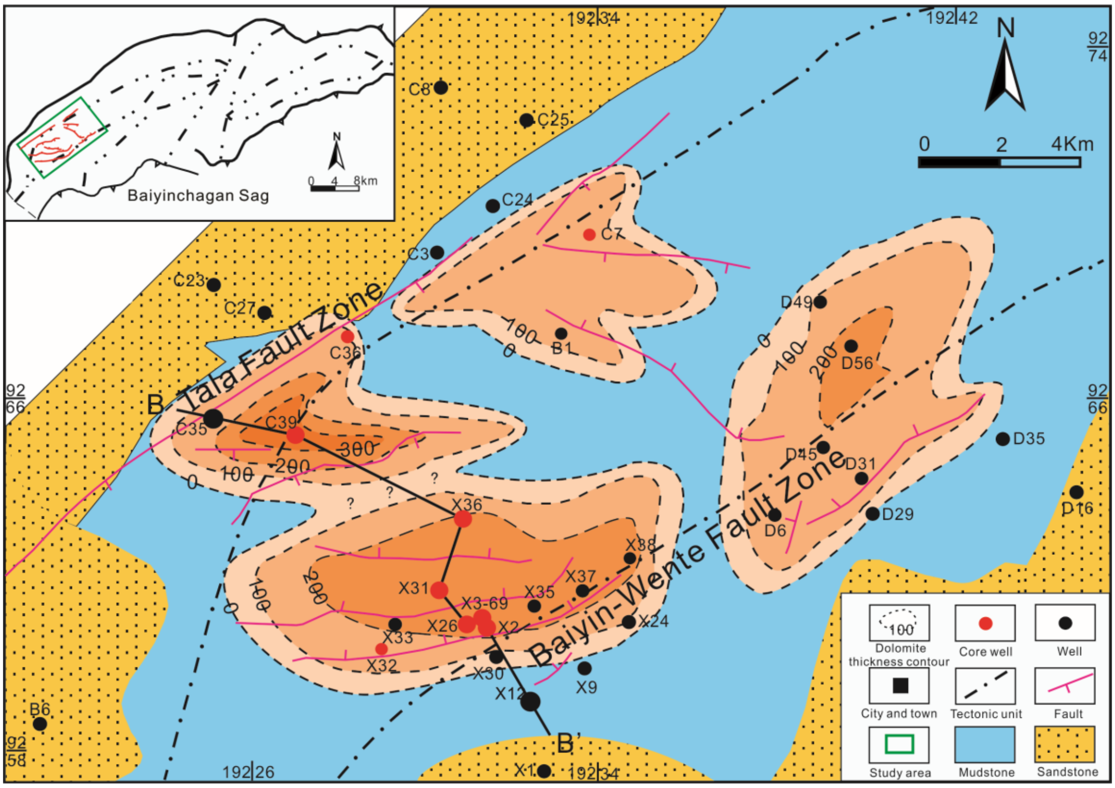

Fig. 2. Isopach map of dolomite of the Upper Member of the Tengger Formation in the study area modified from *Guo et al., (2014)*. The well log response of dolomite-bearing and redeposited terrigenous lacustrine rocks was characterized for cored wells, and used to estimate the total thickness of dolomite-bearing rocks across the basin. Shadings show very localized thickness of dolomite that range from 0 to 300 m. Wells used in cross section (Fig. 3) are shown by large black dots.

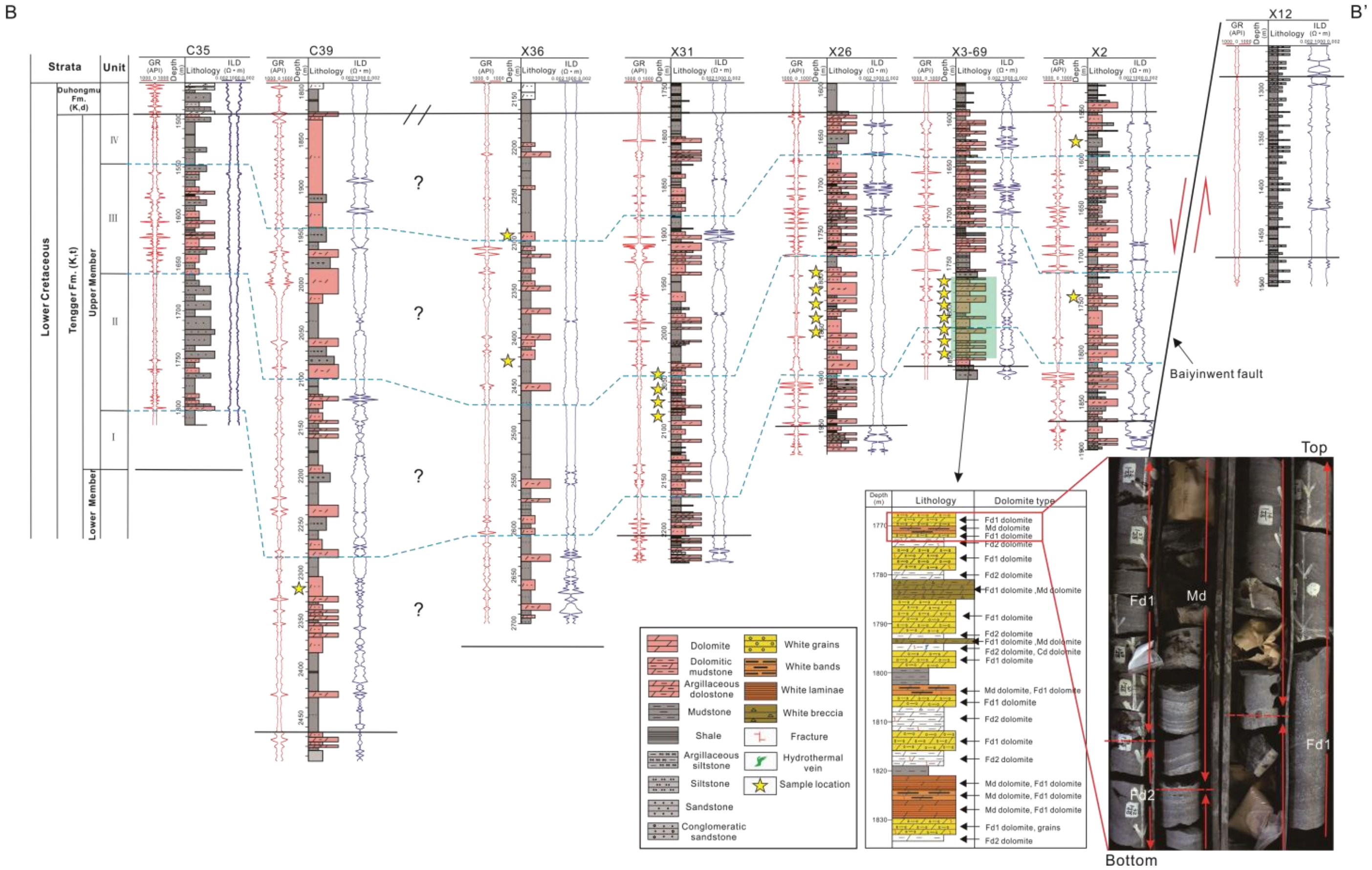

Fig. 3. Regional stratigraphic correlations in the Upper Member of the Tengger Formation along the NW-SE direction in cross-section B-B', the location of the section is given in Fig. 2. In the green rectangle, unique structures and contact relation of dolomite-bearing rock and corresponding dolomite types are described in detail according to core from the Well X3-69. Photos of continuous cores located in the top of Well X3-69 show different types of dolomites with nature of their contact.

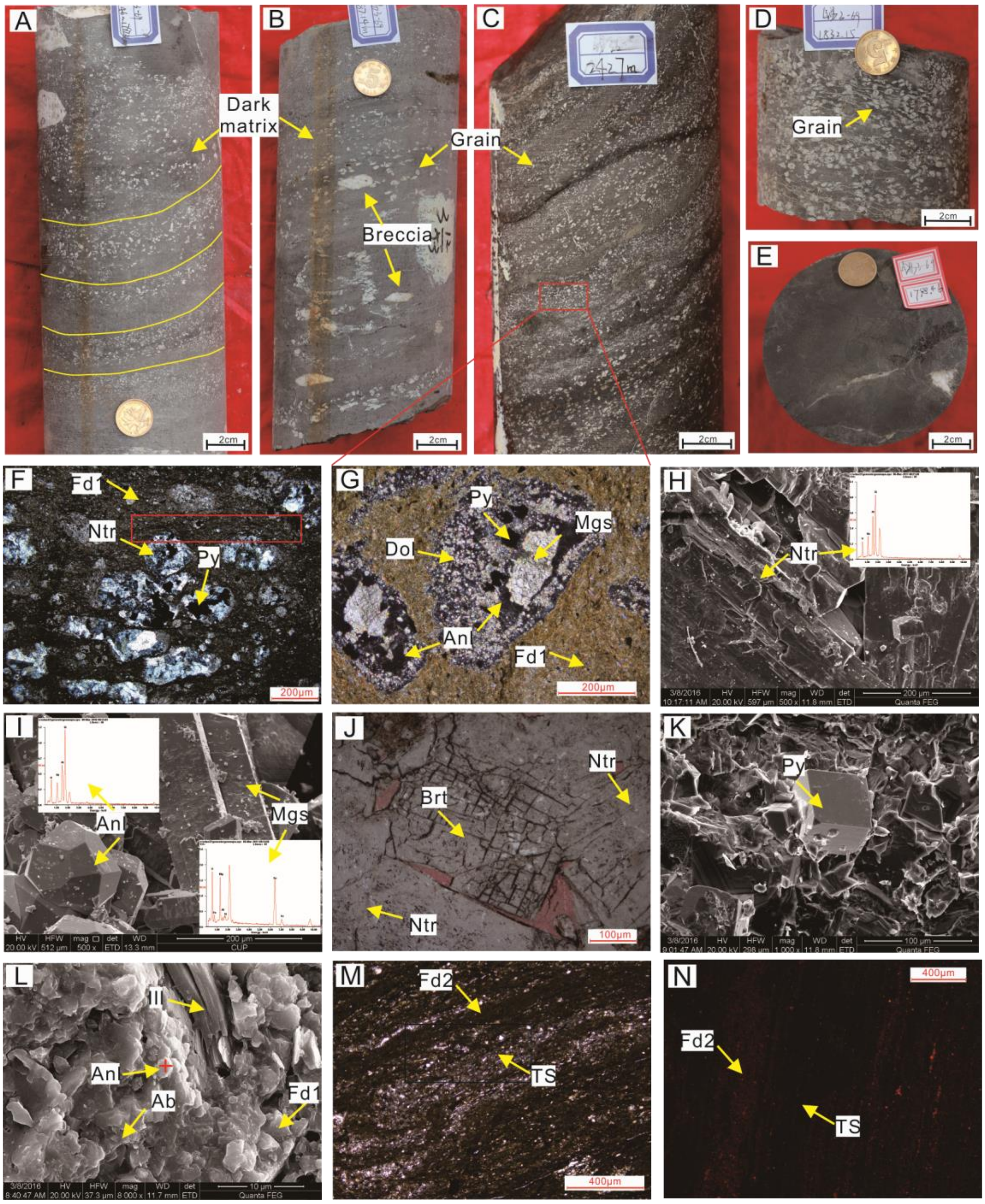

Fig. 4. Core photos, photomicrographs and SEM images showing the petrographic features of the fine-crystalline (Fd1 and Fd2) dolomite and their mineral assemblage within the Upper Member of the Tengger Formation. (A) Core showing white elongated grains composed of natrolite and analcime occurring in the dark-grey matrix of Fd1 dolomite and terrigenous feldspar, and grains gradually growing larger upwards from Well X3-69 at depth of 1795.46 ~ 1797.36 m. (B) Core showing white elongated grains, with larger white breccia clasts scattered in the matrix from Well X3-69 at a depth of 1787.14 m. (C) Core showing white small spherical grains dominated by

analcime and dolomite occurring in the dark-grey matrix from Well X36 at the depth of 2427.0 m. (D) Core showing white irregular and droplet-shape grains made up of natrolite and Fe-bearing magnesite occurring in the in the dark-grey matrix from Well X3-69 at the depth of 1832.15 m. (E) Core showing Fd2 dolomite and terrigenous sediments composing massive argillaceous dolomite from Well X3-69 at the depth of 1798.46 m. (F) Photomicrograph (cross-polarized light) of grains of natrolite and pyrite floating in the matrix, red rectangle showing terrigenous laminae wrapping around grains, from Well X3-69 at the depth of 1771.8 m. (G) SEM image showing euhedral natrolite and forming assemblage from Well X3-69 at the depth of 1784.94 m. (H) Photomicrograph (cross-polarized light) of red rectangle from (C) showing grains composed of analcime with magnesite and dolomite from Well X36 at the depth of 2427.0 m. (I) SEM image showing octahedral analcime and euhedral magnesite from Well X3-69 at the depth of 1782.2 m. (J) SEM image showing cubic pyrite from Well X3-69 at the depth of 1776.8 m. (K) Photomicrograph (plane-polarized light) showing barite in fill of intracrystalline pore within natrolite from Well X26 at the depth of 1824.3 m. (L) Photomicrograph (cross-polarized light) showing laminar structure with alternation of Fd2 and terrigenous sediment layers from Well C7 at the depth of 1206.97 m. (M) SEM image showing anhedral to subhedral Fd1 dolomite and anhedral albite around natrolite from Well X3-69 at the depth of 1771.8 m. (N) CL image showing Fd2 dolomite with a dull red luminescence commixed with terrestrial sediment minerals from Well C7 at the depth of 1206.97 m. Abbreviations are as follows: Ab = albite, Anl = analcime, Brt = barite, Dol = dolomite, Ill = illite, Mgs = magnesite, Ntr = natrolite, Py = pyrite, TS = terrigenous sediments.

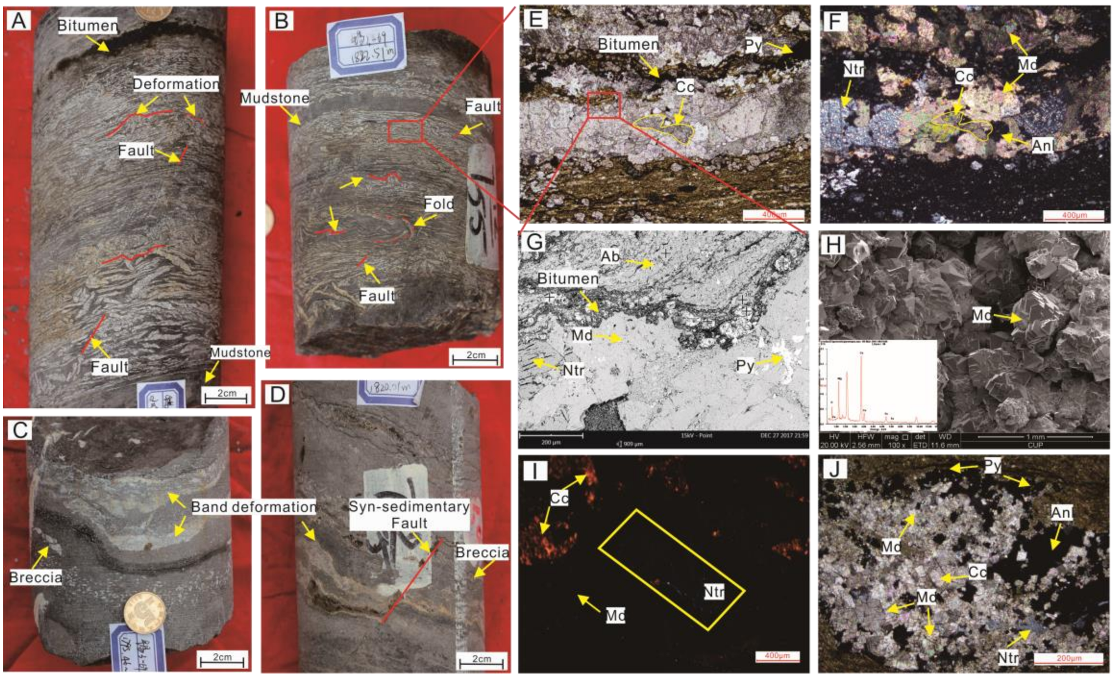

Fig. 5. Core photos and microscopic images showing the petrographic features of the medium-crystalline (Md) dolomite within the Upper Member of the Tengger Formation. (A and B) Core image showing white laminae of Md dolomite alternating with dark-grey terrigenous laminae, and developing syn-sedimentary soft deformation, folding and faults within white laminae from Well X32 and Well X3-69 at the depth of 2074.14 m and 1822.51m, respectively. (C) Core image showing soft deformation within white bands, and white bands breaking into breccia within dolomitic mudstone from Well X3-69 at the depth of 1795.46 m. (D) Core image showing white bands of Md dolomite overlying mudstone and deformation induced by syn-sedimentary faulting from Well26, 1832.24 m. (E and F) Paired photomicrographs (plane-polarized and cross-polarized light) of red rectangle in (B) showing Md dolomite associated with natrolite, analcime and calcite from Well X3-69 at the depth of 1822.51 m. (G) EPMA-BSE image of red rectangle in (E) showing white laminae of Md dolomite accompanying with natrolite and pyrite, and dark-grey laminae composed of subhedral albite from Well X3-69 at the depth of 1822.51 m. (H) SEM image of interlocking Md dolomite assemblage from Well C39 at the depth of 2337.3 m. (I) CL photomicrograph of Md dolomite and natrolite (yellow rectangle) showing no luminescence and intercrystal pores filled by calcite having dull-red luminescence from Well X3-69 at the depth of 1776.8 m. (J) Image from Well 36 at the depth of 2429.2 m. Abbreviations are as follows: Ab = albite, Anl = analcime, Cc =

calcite, Mgs = magnesite, Ntr = natrolite, Py = pyrite.

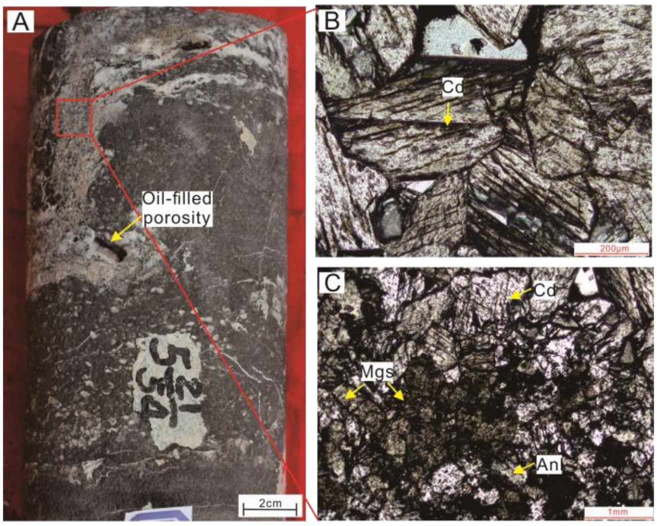

Fig. 6. Images showing the petrographic features of the coarse-crystalline (Cd) dolomite within the Upper Member of the Tengger Formation. (A) Core photo showing massive Cd dolomite filling fractures that crosscut the bedded and postdate Fd1 and Fd2 dolomite and develop into the latter eventually, and develop not fully-filled voids from Well C31 at the depth of 2050.57 m. (B) Photomicrograph (cross-polarized light) of red rectangle in (A) showing intercrystal pores between Cd dolomite (slight blue stained with Alizarin Red-S and K-ferricyanide) from Well C31 at the depth of 2050.57 m. (C) Photomicrograph (plane-polarized light) showing Cd dolomite, cloudy and non-planar crystals size exceeding 1 mm (slight blue stained with Alizarin Red-S and K-ferricyanide) accompanied by abundant magnesite from Well C31 at the depth of 2050.57 m. Abbreviations are as follows: Anl = analcime, Mgs = magnesite.

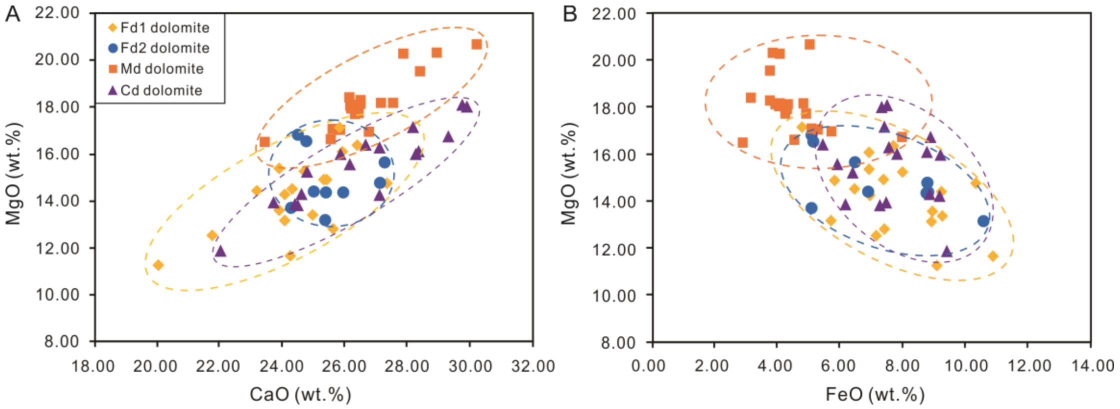

Fig. 7. (A and B) Cross-plots of major-element composition of fine-crystalline (Fd1 and Fd2), medium-crystalline (Md) and coarse-crystalline (Cd) dolomite within the Upper Member of Tengger Formation in the study area, showing relationships between MgO, CaO and FeO.

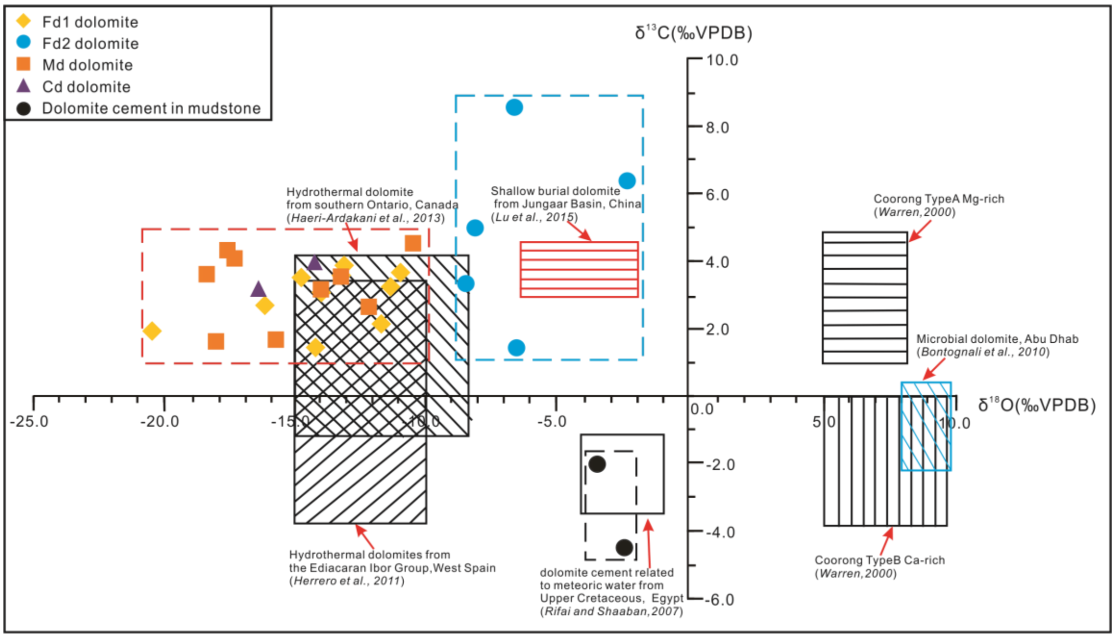

Fig. 8. Cross-plot of $\delta^{18}O$ and $\delta^{13}C$ stable isotopes values including the Upper Member of Tengger Formation dolomite occurrences. Isotopic composition of Fd1 dolomite, Md dolomite and Cd dolomite all lying in the red dashed box, distinguished from Fd2 dolomite lying in blue dashed box and dolomite cement in mudstone lying in black dashed box. The composition of oxygen and carbon isotopes are compared with other dolomites with different genesis, e.g., two hydrothermal dolomites from Canada and West Spain (*Herrero et al., 2011; Haeri-Ardakani et al., 2013*), shallow burial dolomite from Junggar Basin (*Lu et al., 2015*), Coorong Type A Mg-rich and Type B Ca-rich dolomite (*Warren, 2000*), and microbial dolomite from Abu Dhabi (*Bontognali et al., 2010*).

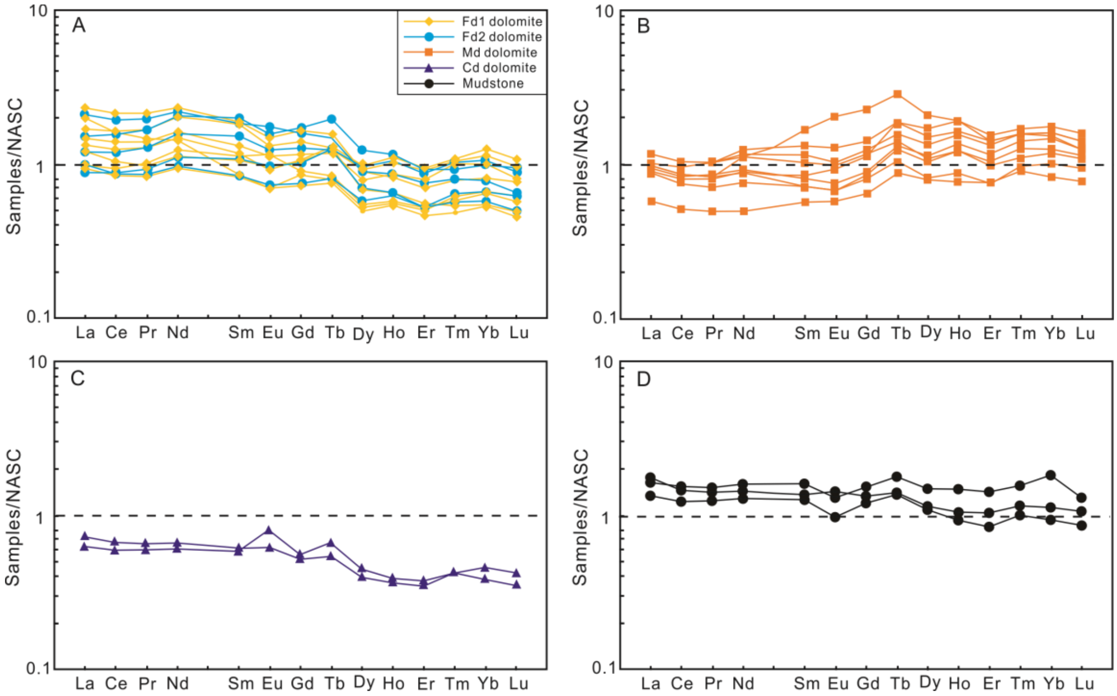

Fig. 9. The NASC normalized REE patterns of dolomites from the Upper Member of Tengger Formation prensent in the study area. The REE_N patterns are divided into four types: (A) the REE_N pattern of Fd1 dolomite and Fd2 dolomite; (B) the REE_N pattern of Md dolomite; (C) the REE_N pattern of Cd dolomite; (D) the REE_N pattern of mudstone.

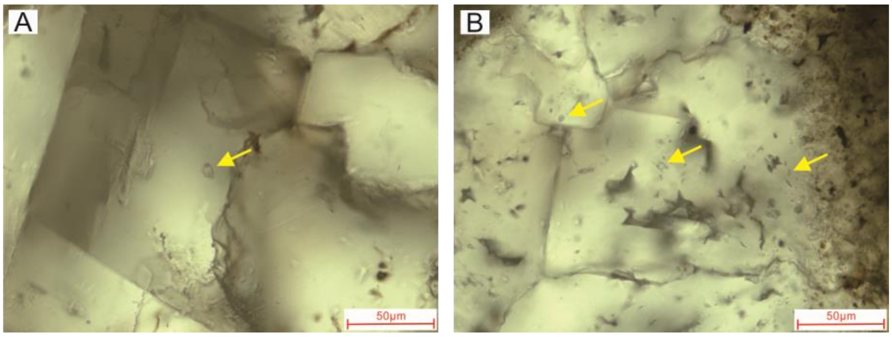

Fig. 10. Photomicrograph of fluid inclusions. (A) Isolated two-phase (liquid-vapour) primary inclusion in Md dolomite with small vapour bubble (yellow arrow); (B) Example of two-phase primary aqueous inclusions in natrolite (yellow arrow).

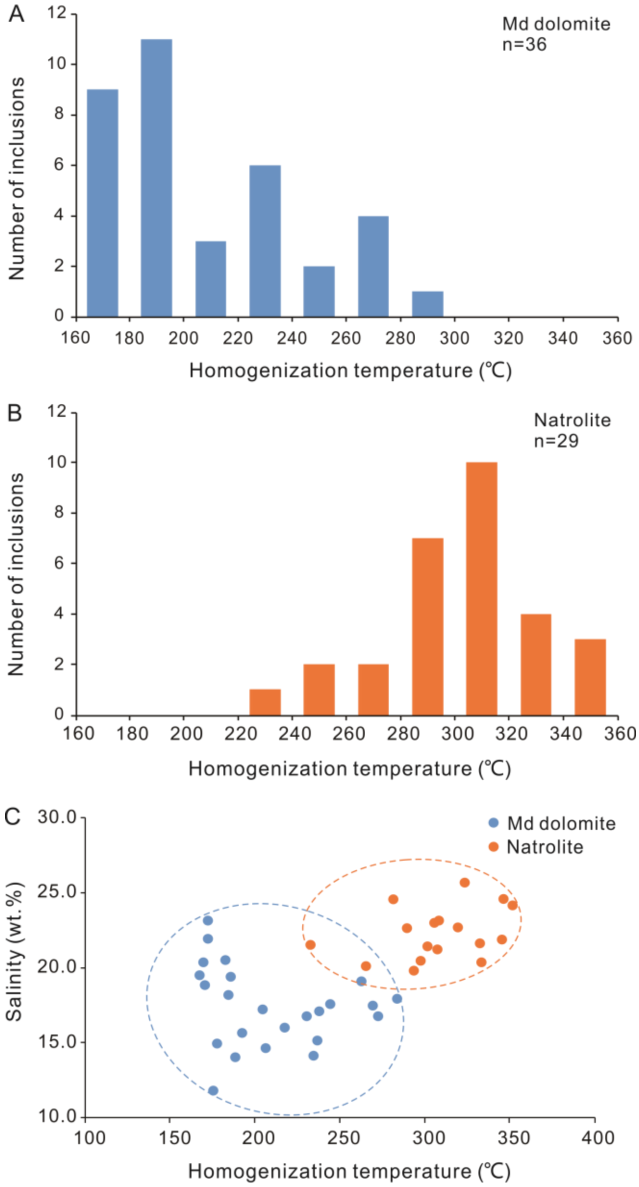

Fig. 11. (A) Histogram of homogenization temperatures of fluid inclusions in Md dolomites. (B) Histogram of homogenization temperatures (T_h) of fluid inclusions in natrolite. (C) Cross-plot of homogenization temperatures (T_h) and salinities of fluid inclusions from Md dolomite and natrolite, showing a trend of increasing temperature and salinity from Md dolomite to natrolite.

Table 1. Summary of EPMA results for dolomites and associated minerals.

	CaO	MgO	FeO	SrO	MnO	ZnO	Na_2O	Al_2O_3	SiO_2	K_2O	TiO_2	Mg/Ca	Si/Al
	(wt.%)	(wt.%)	(wt.%)	(wt.%)	(wt.%)	(wt.%)	(wt.%)	(wt.%)	(wt.%)	(wt.%)	(wt.%)		
Fd1 dolomite													
Mean	24.54	14.13	7.78	0.16	0.22	0.02	0.19	0.33	1.45	0.25	0.07	0.80	\
Standard D	1.66	1.56	1.61	0.10	0.10	0.03	0.14	0.61	2.57	0.49	0.09	0.07	
Maximum	27.35	17.09	10.87	0.37	0.51	0.09	0.50	2.05	9.03	1.65	0.39	0.92	\
Minimum	20.04	11.21	4.79	0.00	0.09	0.00	0.02	0.00	0.13	0.02	0.00	0.67	\
N=number	19												
Fd2 dolomite													
Mean	25.66	14.83	7.42	0.14	0.21	0.02	0.18	0.33	0.83	0.16	0.07	0.81	\
Standard D	1.13	1.17	1.96	0.05	0.10	0.02	0.11	0.29	0.62	0.15	0.08	0.08	\
Maximum	27.26	16.80	10.56	0.21	0.38	0.07	0.37	0.77	1.88	0.51	0.25	0.95	\
Minimum	24.27	13.13	5.06	0.07	0.09	0.00	0.06	0.03	0.30	0.04	0.01	0.72	\
N=number	10												
Md dolomite													
Mean	26.84	18.10	4.47	0.08	0.25	0.02	0.22	0.27	1.09	0.16	0.10	0.94	\
Standard D	1.51	1.24	1.08	0.05	0.07	0.02	0.20	0.69	2.23	0.30	0.30	0.04	
Maximum	30.18	20.66	7.96	0.19	0.39	0.06	0.83	3.07	10.13	1.35	1.38	1.01	\
Minimum	23.41	16.48	2.88	0.00	0.08	0.00	0.00	0.00	0.08	0.01	0.00	0.80	\
N=number	35												
Cd dolomite													
Mean	26.50	15.44	7.68	0.08	0.30	0.02	0.09	0.02	0.13	0.09	0.05	0.81	\
Standard D	2.28	1.66	1.23	0.08	0.05	0.02	0.12	0.03	0.15	0.12	0.18	0.04	\
Maximum	29.89	18.02	9.40	0.21	0.37	0.07	0.45	0.13	0.68	0.46	0.75	0.86	\
Minimum	22.01	11.81	5.43	0.00	0.21	0.00	0.01	0.00	0.04	0.01	0.00	0.73	\
N=number	17												
Natrolite													
Mean	0.07	0.03	0.07	\	\	0.02	12.86	27.28	49.46	0.03	0.02	\	1.82
Standard D	0.08	0.02	0.06	0.00	0.01	0.02	3.56	1.89	2.47	0.02	0.02	\	0.05
Maximum	0.39	0.10	0.22	\	\	0.08	17.49	30.71	54.40	0.09	0.06	\	1.88
Minimum	0.00	0.00	0.00	\	\	0.00	6.58	22.66	42.64	0.01	0.00	\	1.71
N=number	21												
Analcime													
Mean	0.13	0.06	0.11	\	\	0.02	11.19	21.53	55.65	0.48	0.02	\	2.59
Standard D	0.07	0.04	0.07	0.00	0.01	0.02	2.87	1.16	2.06	1.09	0.04	\	0.13
Maximum	0.33	0.17	0.28	\	\	0.05	15.25	23.68	58.75	5.13	0.16	\	2.88
Minimum	0.04	0.01	0.01	\	\	0.00	6.65	19.49	52.05	0.03	0.00	\	2.33
N=number	24												
Fe-bearing magnesite													
Mean	0.37	15.92	32.51	0.00	0.53	0.03	0.13	0.08	0.26	0.03	0.02	\	\
Standard D	0.08	3.64	0.13	0.34	0.00	0.04	0.37	0.03	0.10	3.81	0.04	\	\
Maximum	1.09	21.05	36.43	0.01	0.64	0.10	0.36	0.36	1.21	0.15	0.11	\	\
Minimum	0.04	11.27	26.75	0.00	0.36	0.00	0.08	0.00	0.06	0.00	0.00	\	\
N=number	10												

Table 2. Summary of carbon and oxygen isotopic compositions and REE contents of dolomites.

	$\delta^{18}O$	$\delta^{13}C$	La	Ce	Pr	Nd	Sm	Eu	Gd	Tb	Dy	Ho	Er	Tm	Yb	Lu	Y	ΣREE	LREE	HREE	LREE/HRI	La_N/Yb_N	δEu	δCe
	(VPDB)	(VPDB)	(ppm)	(ppm)	(ppm)	(ppm)	(ppm)	(ppm)	(ppm)	(ppm)	(ppm)	(ppm)	(ppm)	(ppm)	(ppm)	(ppm)	(ppm)	(ppm)	(ppm)	(ppm)				
Fd1 dolomite																								
Mean	-13.5	2.8	46.80	90.19	10.59	40.89	7.38	1.23	5.69	0.88	4.22	0.79	2.28	0.38	2.45	0.32	23.28	214.08	197.07	17.01	11.85	2.09	0.88	0.95
Standard Deviation	2.2	0.9	14.01	26.76	3.10	11.62	2.19	0.31	1.48	0.21	1.06	0.21	0.61	0.11	0.77	0.09	6.72	58.04	56.32	3.77	3.20	0.85	0.09	0.01
Maximum	-11.0	3.7	72.70	142.00	16.70	62.50	11.00	1.75	8.58	1.24	5.66	1.14	3.19	0.54	3.72	0.47	33.50	328.08	306.65	21.43	17.89	3.27	1.10	0.97
Minimum	-18.0	1.4	29.50	56.60	6.54	25.30	4.82	0.82	3.75	0.60	2.85	0.56	1.57	0.24	1.59	0.20	15.70	135.15	123.59	11.57	7.19	1.02	0.79	0.94
N=number of	9																							
Fd2 dolomite																								
Mean	-6.8	4.9	42.50	86.44	10.66	43.00	8.68	1.50	6.66	1.07	5.10	0.91	2.47	0.40	2.43	0.32	25.58	212.14	192.77	19.37	10.00	1.83	0.90	0.96
Standard Deviation	1.5	2.5	14.03	28.21	3.38	13.37	2.60	0.45	1.91	0.30	1.33	0.22	0.58	0.09	0.55	0.07	6.34	64.14	61.19	4.45	2.28	0.66	0.05	0.01
Maximum	-4.3	8.6	66.80	131.00	15.60	59.80	11.80	2.08	9.11	1.56	7.25	1.21	3.17	0.51	3.16	0.42	33.30	307.56	286.28	26.15	13.46	2.85	0.99	0.97
Minimum	-8.5	1.4	28.00	57.90	6.83	26.40	5.03	0.88	3.95	0.64	3.37	0.65	1.80	0.28	1.71	0.22	17.90	141.25	128.24	13.02	6.56	0.89	0.83	0.93
N=number of	5																							
Md dolomite																								
Mean	-14.8	3.4	31.25	59.38	6.95	27.11	6.09	1.23	6.27	1.29	7.70	1.51	4.08	0.69	4.22	0.56	43.09	158.32	132.01	26.31	5.26	0.77	0.90	0.95
Standard Deviation	2.5	0.8	3.57	7.18	0.90	4.27	1.84	0.49	2.21	0.42	2.19	0.35	0.84	0.12	0.69	0.09	10.29	18.72	16.04	6.40	1.11	0.16	0.06	0.01
Maximum	-10.5	4.5	37.30	70.70	8.12	33.20	9.84	2.37	11.50	2.25	11.90	1.98	5.22	0.84	5.15	0.69	59.50	180.81	153.78	38.64	6.69	1.00	1.02	0.96
Minimum	-18.4	1.7	27.30	49.80	5.52	20.50	4.24	0.79	4.20	0.84	4.69	0.91	2.55	0.48	2.99	0.42	25.90	126.13	109.05	17.08	3.37	0.54	0.84	0.93
N=number of	10																							
Cc dolomite																								
Mean	-15.3	3.5	21.45	42.80	5.07	19.45	3.59	0.87	2.98	0.50	2.38	0.45	1.20	0.21	1.31	0.17	12.40	102.41	93.23	9.19	10.20	1.66	1.21	0.97
Standard Deviation	1.6	0.5	2.19	3.96	0.38	1.34	0.18	0.12	0.11	0.05	0.21	0.02	0.05	0.00	0.17	0.02	0.14	7.31	7.94	0.63	1.56	0.38	0.18	0.00
Maximum	-14.2	3.9	23.00	45.60	5.34	20.40	3.72	0.95	3.06	0.53	2.52	0.47	1.23	0.21	1.43	0.19	12.50	107.58	98.84	9.63	11.30	1.93	1.34	0.97
Minimum	-16.4	3.2	19.90	40.00	4.80	18.50	3.46	0.78	2.90	0.46	2.23	0.43	1.16	0.21	1.19	0.16	12.30	97.24	87.61	8.74	9.10	1.39	1.08	0.96
N=number of	2																							
Mudstone																								
Mean	-3.0	-3.3	49.03	94.17	11.12	43.70	8.44	1.55	7.43	1.29	6.86	1.35	3.60	0.60	4.03	0.49	38.17	233.64	208.00	25.64	8.23	1.30	0.89	0.95
Standard Deviation	0.6	1.8	6.63	10.68	1.09	4.70	1.05	0.29	0.93	0.19	1.20	0.34	0.97	0.14	1.46	0.10	8.03	27.65	23.12	5.30	0.97	0.35	0.15	0.03
Maximum	-2.5	-2.0	54.60	103.00	12.10	48.50	9.60	1.79	8.42	1.51	8.23	1.74	4.65	0.76	5.68	0.59	46.90	257.21	225.63	31.58	9.03	1.56	1.06	0.98
Minimum	-3.4	-4.6	41.70	82.30	9.95	39.10	7.56	1.22	6.57	1.16	6.02	1.09	2.75	0.48	2.91	0.39	31.10	203.20	181.83	21.37	7.15	0.90	0.79	0.92
N=number of	3																							

Table 3. Fluid-inclusion microthermometry of medium-crystalline dolomite and natrolite.

Sample	Host mineral	Location	Number of inclusions	T_{h}(℃)			T_{m}(℃)			Salinity (eq. wt% NaCl)		
				Maximum	Minimum	Mean	Maximum	Minimum	Mean	Maximum	Minimum	Mean
X31-2080.04	Md dolomite	1	3	177	173	175	-8.1	-11	-9.6	15.0	11.8	13.4
	Md dolomite	2	3	192	181	185	-11.7	-11.7	-11.7	15.7	15.7	15.7
	Md dolomite	3	1	217	217	217	-12.1	-12.1	-12.1	16.1	16.1	16.1
	Md dolomite	4	2	206	192	199	-10.7	-10.7	-10.7	14.7	14.7	14.7
	Md dolomite	5	1	237	237	237	-13.2	-13.2	-13.2	17.1	17.1	17.1
	Md dolomite	6	4	190	169	178	-15.3	-17.2	-16.3	20.4	18.9	19.6
X3-69-1822.51	Md dolomite	1	1	204	204	204	-13.4	-13.4	-13.4	17.3	17.3	17.3
	Md dolomite	2	3	177	167	172	-16.1	-19.4	-17.8	22.0	19.5	20.7
	Md dolomite	3	2	184	182	183	-14.5	-17.4	-16.0	22.0	19.5	20.7
	Md dolomite	4	3	185	172	180	-16	-21.2	-18.6	23.2	19.5	21.3
X3-69-1826.6	Md dolomite	1	2	238	234	236	-10.2	-10.2	-10.2	14.2	14.2	14.2
	Md dolomite	2	1	188	188	188	-10.1	-10.1	-10.1	14.0	14.0	14.0
	Md dolomite	3	2	231	230	231	-12.9	-12.9	-12.9	16.8	16.8	16.8
	Md dolomite	4	3	262	244	253	-13.8	-15.6	-14.7	19.1	17.6	18.4
X32-2074.14	Md dolomite	1	2	283	269	276	-14.2	-14.2	-14.2	18.0	18.0	18.0
	Md dolomite	2	1	236	236	236	-11.2	-11.2	-11.2	15.2	15.2	15.2
	Md dolomite	3	2	272	269	271	-12.9	-13.7	-13.3	17.5	16.8	17.2
X32-1816.6	Natrolite	1	2	307	293	300	-16.5	-18.4	-17.5	21.3	19.8	20.6
	Natrolite	2	3	322	308	316	-20.5	-21.3	-20.9	23.2	22.7	22.9
	Natrolite	3	2	289	286	288	-20.4	-20.4	-20.4	22.7	22.7	22.7
	Natrolite	4	2	314	304	309	\	\	\	\	\	\
	Natrolite	5	3	305	292	300	-21.1	-21.1	-21.1	23.1	23.1	23.1
X3-69-1832	Natrolite	1	1	265	265	265	-16.9	-16.9	-16.9	20.2	20.2	20.2
	Natrolite	2	1	297	297	297	-17.4	-17.4	-17.4	20.5	20.5	20.5
	Natrolite	3	2	332	320	326	-19	-19	-19.0	21.7	21.7	21.7
	Natrolite	4	2	345	333	339	-17.2	-19.3	-18.3	21.9	20.4	21.1
	Natrolite	5	1	318	318	318	\	\	\	\	\	\
X3-69-1831.75	Natrolite	1	2	245	232	239	-18.8	-18.8	-18.8	21.5	21.5	21.5
	Natrolite	2	1	323	323	323	-25.2	-25.2	-25.2	25.7	25.7	25.7
	Natrolite	3	1	271	271	271	\	\	\	\	\	\
	Natrolite	4	1	281	281	281	-23.4	-23.4	-23.4	24.6	24.6	24.6
X26-1816.33	Natrolite	1	1	256	256	256	\	\	\	\	\	\
	Natrolite	2	1	287	287	287	\	\	\	\	\	\
	Natrolite	3	2	351	346	349	-22.8	-23.4	-23.1	24.6	24.2	24.4
	Natrolite	4	1	301	301	301	-18.7	-18.7	-18.7	21.5	21.5	21.5

Table S1. Thickness statistics of observed cores in the study area.

NO.	Well name	Stratigraphy	Top depth of core (m)	Bottom depth of core (m)	Total length of core (m)	Thin section NO.
1	X3-69	Upper Member of the Tengger Fm.	1767.3	1834.36	67.06	28
2	X36	Upper Member of the Tengger Fm.	2290.92	2299.16	16.58	11
			2424.2	2432.54		
3	X2	Upper Member of the Tengger Fm.	1577.3	1585	31.28	5
			1740.41	1748		
			2113.34	2121.33		
			2250	2258		
4	X26	Upper Member of the Tengger Fm.	1775.2	1851.43	76.23	18
5	X31	Upper Member of the Tengger Fm.	2011.14	2083.14	78.93	19
			2993.07	3000		
6	X32	Upper Member of the Tengger Fm.	1817.6	1834.55	16.95	6
7	C36	Upper Member of the Tengger Fm.	1679.83	1687.83	15	1
			2261	2268		
8	C39	Upper Member of the Tengger Fm.	2336.52	2341.27	10.36	5
		Lower Member of the Tengger Fm.	2888.49	2894.1		
Sum					312.39	93

Table S2. Detailed carbon and oxygen isotopic compositions and REE contents of dolomites.

Sample	Petrography	$\delta^{18}O$	$\delta^{13}C$	La	Ce	Pr	Nd	Sm	Eu	Gd	Tb	Dy	Ho	Er	Tm	Yb	Lu	Y	ΣREE	LREE	HREE	REE/HRE	La_N/Yb_N	δEu	δCe
		(VPDB)	(VPDB)	(ppm)	(ppm)	(ppm)	(ppm)	(ppm)	(ppm)	(ppm)	(ppm)	(ppm)	(ppm)	(ppm)	(ppm)	(ppm)	(ppm)	(ppm)	(ppm)	(ppm)	(ppm)				
X26-1816.33	Fd1 dolomite	\	\	31.00	62.40	7.93	33.20	6.67	1.34	4.68	0.66	3.13	0.59	1.75	0.29	1.92	0.25	16.90	155.81	142.54	13.27	10.75	1.62	1.10	0.94
X26-1818.4		-14.0	3.2	52.60	108.00	13.10	54.20	10.70	1.55	7.26	1.00	3.90	0.67	1.88	0.27	1.61	0.22	18.70	256.95	240.15	16.80	14.29	3.27	0.80	0.97
X26-1832		-13.2	3.6	29.50	56.60	6.54	25.30	4.82	0.83	3.75	0.60	3.05	0.57	1.57	0.24	1.59	0.20	15.70	135.15	123.59	11.57	10.68	1.86	0.89	0.96
X31-2032.5		-14.2	1.4	61.60	108.00	11.60	39.10	5.08	0.82	4.39	0.63	2.85	0.56	1.69	0.30	1.95	0.27	17.10	238.84	226.20	12.65	17.89	3.16	0.79	0.95
X31-2046.98		-14.8	3.5	72.70	142.00	16.70	62.50	11.00	1.75	8.58	1.24	5.22	0.86	2.39	0.39	2.42	0.34	24.90	328.08	306.65	21.43	14.31	3.01	0.82	0.96
X36-2429.2		-18.0	1.6	46.80	92.70	11.00	43.50	7.72	1.33	5.97	0.93	4.57	0.89	2.71	0.50	2.99	0.36	27.00	221.96	203.05	18.91	10.74	1.57	0.90	0.96
X3-69-1772.8		-11.4	3.2	42.20	82.80	10.10	39.40	6.87	1.09	5.53	0.98	5.34	1.06	3.08	0.52	3.38	0.42	32.40	202.77	182.46	20.31	8.98	1.25	0.81	0.95
X3-69-1778.5		-11.0	3.7	38.00	69.00	7.72	29.90	6.18	1.14	5.39	1.02	5.66	1.14	3.19	0.54	3.72	0.47	33.50	173.07	151.94	21.13	7.19	1.02	0.90	0.95
X3-69-1826.01		-11.7	2.1	\	\	\	\	\	\	\	\	\	\	\	\	\	\	\	\	\	\	\	\	\	\
Mean		-13.5	2.8	46.80	90.19	10.59	40.89	7.38	1.23	5.69	0.88	4.22	0.79	2.28	0.38	2.45	0.32	23.28	214.08	197.07	17.01	11.85	2.09	0.88	0.95
Standard Deviation		2.2	0.9	14.01	26.76	3.10	11.62	2.19	0.31	1.48	0.21	1.06	0.21	0.61	0.11	0.77	0.09	6.72	58.04	56.32	3.77	3.20	0.85	0.09	0.01
Maximum		-11.0	3.7	72.70	142.00	16.70	62.50	11.00	1.75	8.58	1.24	5.66	1.14	3.19	0.54	3.72	0.47	33.50	328.08	306.65	21.43	17.89	3.27	1.10	0.97
Minimum		-18.0	1.4	29.50	56.60	6.54	25.30	4.82	0.82	3.75	0.60	2.85	0.56	1.57	0.24	1.59	0.20	15.70	135.15	123.59	11.57	7.19	1.02	0.79	0.94
X32-1818.6	Fd2 dolomite	-6.5	1.4	28.00	58.30	7.36	29.90	6.42	1.16	5.28	0.99	5.58	1.09	2.99	0.51	3.16	0.40	31.80	151.14	131.14	20.00	6.56	0.89	0.91	0.96
X3-69-1791.44		-4.3	6.4	48.50	105.00	13.30	55.80	11.80	1.89	9.11	1.56	7.25	1.21	3.17	0.47	2.96	0.42	33.30	262.44	236.29	26.15	9.04	1.64	0.83	0.97
X3-69-1801.76		-8.5	3.3	66.80	131.00	15.60	59.80	11.00	2.08	8.37	1.18	5.19	0.91	2.58	0.40	2.35	0.30	25.90	307.56	286.28	21.28	13.46	2.85	0.99	0.96
X3-69-1808.42		-8.1	5.0	31.20	57.90	6.83	26.40	5.03	0.88	3.95	0.64	3.37	0.65	1.81	0.33	1.99	0.28	17.90	141.25	128.24	13.02	9.85	1.57	0.90	0.93
X3-69-1812.95(2)		-6.6	8.6	38.00	80.00	10.20	43.10	9.13	1.47	6.61	0.99	4.13	0.68	1.80	0.28	1.71	0.22	19.00	198.32	181.90	16.42	11.08	2.22	0.87	0.96
Mean		-6.8	4.9	42.50	86.44	10.66	43.00	8.68	1.50	6.66	1.07	5.10	0.91	2.47	0.40	2.43	0.32	25.58	212.14	192.77	19.37	10.00	1.83	0.90	0.96
Standard Deviation		1.5	2.5	14.03	28.21	3.38	13.37	2.60	0.45	1.91	0.30	1.33	0.22	0.58	0.09	0.55	0.07	6.34	64.14	61.19	4.45	2.28	0.66	0.05	0.01
Maximum		-4.3	8.6	66.80	131.00	15.60	59.80	11.80	2.08	9.11	1.56	7.25	1.21	3.17	0.51	3.16	0.42	33.30	307.56	286.28	26.15	13.46	2.85	0.99	0.97
Minimum		-8.5	1.4	28.00	57.90	6.83	26.40	5.03	0.88	3.95	0.64	3.37	0.65	1.80	0.28	1.71	0.22	17.90	141.25	128.24	13.02	6.56	0.89	0.83	0.93
X2-1743.41	Md dolomite	-17.3	4.0	\	\	\	\	\	\	\	\	\	\	\	\	\	\	\	\	\	\	\	\	\	\
X3-69-1776.8		-13.2	3.5	30.10	55.50	6.52	24.60	4.78	0.89	4.60	1.03	6.52	1.40	3.97	0.71	4.39	0.55	40.80	145.56	122.39	23.17	5.28	0.69	0.87	0.93
X3-69-1822.51		-10.5	4.5	27.30	55.00	6.74	29.10	9.84	2.37	11.50	2.25	11.90	1.97	4.78	0.78	4.81	0.65	53.50	168.99	130.35	38.64	3.37	0.57	1.02	0.96
X31-2076.84		-15.7	1.7	\	\	\	\	\	\	\	\	\	\	\	\	\	\	\	\	\	\	\	\	\	\
X31-2080.04		-12.2	2.7	32.10	63.90	7.94	33.20	7.78	1.50	7.27	1.46	8.68	1.69	4.76	0.77	4.71	0.62	49.20	176.38	146.42	29.96	4.89	0.68	0.91	0.94
X3-69-1771.3		-18.4	3.2	28.00	53.70	6.31	23.60	5.00	1.10	5.77	1.46	9.83	1.98	5.22	0.84	5.15	0.69	59.50	148.64	117.71	30.93	3.81	0.54	0.94	0.95
X3-69-1771.7		-13.2	3.9	30.50	57.00	6.45	23.80	4.26	0.79	4.41	0.97	6.02	1.24	3.32	0.55	3.49	0.48	35.50	143.29	122.80	20.48	6.00	0.87	0.84	0.96
X3-69-1785.5		-16.2	2.7	28.20	49.80	5.52	20.50	4.24	0.79	4.20	0.84	4.69	0.91	2.55	0.48	2.99	0.42	25.90	126.13	109.05	17.08	6.39	0.94	0.86	0.94
X3-69-1831.75		-14.0	3.1	37.30	70.70	8.03	30.50	6.09	1.16	6.01	1.10	6.24	1.26	3.54	0.63	3.72	0.50	34.80	176.78	153.78	23.00	6.69	1.00	0.88	0.96
X31-2083.9		-17.6	4.2	36.50	69.40	8.12	31.60	6.72	1.22	6.37	1.23	7.71	1.61	4.53	0.78	4.47	0.55	45.50	180.81	153.56	27.25	5.64	0.82	0.85	0.95
Mean		-14.8	3.4	31.25	59.38	6.95	27.11	6.09	1.23	6.27	1.29	7.70	1.51	4.08	0.69	4.22	0.56	43.09	158.32	132.01	26.31	5.26	0.77	0.90	0.95
Standard Deviation		2.5	0.8	3.57	7.18	0.90	4.27	1.84	0.49	2.21	0.42	2.19	0.35	0.84	0.12	0.69	0.09	10.29	18.72	16.04	6.40	1.11	0.16	0.06	0.01
Maximum		-10.5	4.5	37.30	70.70	8.12	33.20	9.84	2.37	11.50	2.25	11.90	1.98	5.22	0.84	5.15	0.69	59.50	180.81	153.78	38.64	6.69	1.00	1.02	0.96
Minimum		-18.4	1.7	27.30	49.80	5.52	20.50	4.24	0.79	4.20	0.84	4.69	0.91	2.55	0.48	2.99	0.42	25.90	126.13	109.05	17.08	3.37	0.54	0.84	0.93
X26-1829.38	Cd dolomite	-14.2	3.9	23.00	45.60	5.34	20.40	3.72	0.78	2.90	0.46	2.23	0.43	1.16	0.21	1.19	0.16	12.50	107.58	98.84	8.74	11.30	1.93	1.08	0.97
X31-2050.57		-16.4	3.2	19.90	40.00	4.80	18.50	3.46	0.95	3.06	0.53	2.52	0.47	1.23	0.21	1.43	0.19	12.30	97.24	87.61	9.63	9.10	1.39	1.34	0.96
Mean		-15.3	3.5	21.45	42.80	5.07	19.45	3.59	0.87	2.98	0.50	2.38	0.45	1.20	0.21	1.31	0.17	12.40	102.41	93.23	9.19	10.20	1.66	1.21	0.97
Standard Deviation		1.6	0.5	2.19	3.96	0.38	1.34	0.18	0.12	0.11	0.05	0.21	0.02	0.05	0.00	0.17	0.02	0.14	7.31	7.94	0.63	1.56	0.38	0.18	0.00
Maximum		-14.2	3.9	23.00	45.60	5.34	20.40	3.72	0.95	3.06	0.53	2.52	0.47	1.23	0.21	1.43	0.19	12.50	107.58	98.84	9.63	11.30	1.93	1.34	0.97
Minimum		-16.4	3.2	19.90	40.00	4.80	18.50	3.46	0.78	2.90	0.46	2.23	0.43	1.16	0.21	1.19	0.16	12.30	97.24	87.61	8.74	9.10	1.39	1.08	0.96
X31-2993.67	Mudstone	-3.4	-2.0	41.70	82.30	9.95	39.10	7.56	1.22	6.57	1.16	6.02	1.09	2.75	0.48	2.91	0.39	31.10	203.20	181.83	21.37	8.51	1.43	0.79	0.95
X2-1747.1		-2.5	-4.6	50.80	103.00	12.10	48.50	9.60	1.63	8.42	1.51	8.23	1.74	4.65	0.76	5.68	0.59	46.90	257.21	225.63	31.58	7.15	0.90	0.83	0.98
X32-1840.51		\	\	54.60	97.20	11.30	43.50	8.15	1.79	7.30	1.19	6.32	1.23	3.39	0.56	3.50	0.48	36.50	240.51	216.54	23.97	9.03	1.56	1.06	0.92
Mean		-3.0	-3.3	49.03	94.17	11.12	43.70	8.44	1.55	7.43	1.29	6.86	1.35	3.60	0.60	4.03	0.49	38.17	233.64	208.00	25.64	8.23	1.30	0.89	0.95
Standard Deviation		0.6	1.8	6.63	10.68	1.09	4.70	1.05	0.29	0.93	0.19	1.20	0.34	0.97	0.14	1.46	0.10	8.03	27.65	23.12	5.30	0.97	0.35	0.15	0.03
Maximum		-2.5	-2.0	54.60	103.00	12.10	48.50	9.60	1.79	8.42	1.51	8.23	1.74	4.65	0.76	5.68	0.59	46.90	257.21	225.63	31.58	9.03	1.56	1.06	0.98
Minimum		-3.4	-4.6	41.70	82.30	9.95	39.10	7.56	1.22	6.57	1.16	6.02	1.09	2.75	0.48	2.91	0.39	31.10	203.20	181.83	21.37	7.15	0.90	0.79	0.92